



1 **Estimation of Reactive Inorganic Iodine Fluxes in the Indian and Southern Ocean Marine**  
2 **Boundary Layer**

3 Swaleha Inamdar<sup>1,2</sup>, Liselotte Tinel<sup>3</sup>, Rosie Chance<sup>3</sup>, Lucy J. Carpenter<sup>3</sup>, Prabhakaran Sabu<sup>4</sup>,  
4 Racheal Chacko<sup>4</sup>, Sarat C. Tripathy<sup>4</sup>, Anvita U. Kerkar<sup>4</sup>, Alok K. Sinha<sup>4</sup>, Parli Venkateswaran  
5 Bhaskar<sup>4</sup>, Amit Sarkar<sup>4,5</sup>, Rajdeep Roy<sup>6</sup>, Tomas Sherwen<sup>3,7</sup>, Carlos Cuevas<sup>8</sup>, Alfonso Saiz-  
6 Lopez<sup>8</sup>, Kirpa Ram<sup>2</sup> and Anoop S. Mahajan<sup>1\*</sup>

7 <sup>1</sup>Centre for Climate Change Research, Indian Institute of Tropical Meteorology, Dr Homi  
8 Bhabha Road, Pashan, Pune, 411 008, India

9 <sup>2</sup>Institute of Environment and Sustainable Development, Banaras Hindu University, Varanasi,  
10 221 005, India

11 <sup>3</sup>Wolfson Atmospheric Chemistry Laboratories, Department of Chemistry, University of York,  
12 YO10 5DD, UK

13 <sup>4</sup>National Centre for Polar and Ocean Research, Goa, 403 804, India

14 <sup>5</sup>Environment and Life Sciences Research Centre, Kuwait Institute for Scientific Research  
15 Centre, Al-Jaheth Street, Shuwaikh, 13109, Kuwait

16 <sup>6</sup>National Remote Sensing Centre, Department of Space Government of India Balanagar,  
17 Hyderabad, 500 037, India

18 <sup>7</sup>National Centre for Atmospheric Science, University of York, York YO10 5DD, UK

19 <sup>8</sup>Department of Atmospheric Chemistry and Climate, Institute of Physical Chemistry  
20 Rocasolano, CSIC, Madrid, Spain.

21 \* Corresponding author: Anoop S. Mahajan ([anoop@tropmet.res.in](mailto:anoop@tropmet.res.in)); phone: +91 20 2590 4526



22 **Abstract**

23 Iodine chemistry has noteworthy impacts on the oxidising capacity of the marine boundary  
24 layer (MBL) through the depletion of ozone ( $O_3$ ) and changes to  $HO_x$  (OH/ $HO_2$ ) and  $NO_x$   
25 ( $NO/NO_2$ ) ratios. Hitherto, studies have shown that the reaction of atmospheric  $O_3$  with surface  
26 seawater iodide (I<sup>-</sup>) contributes to the flux of iodine species into the MBL mainly as hypoiodous  
27 acid (HOI) and molecular iodine ( $I_2$ ). Here, we present the first concomitant observations of  
28 iodine oxide (IO),  $O_3$  in the gas phase, and sea surface iodide concentrations. The results from  
29 three field campaigns in the Indian Ocean and the Southern Ocean during 2014-2017 are used  
30 to compute reactive iodine fluxes to the MBL. Observations of atmospheric IO by MAX-  
31 DOAS show active iodine chemistry in this environment, with IO values up to 1 pptv (parts  
32 per trillion by volume) below latitudes of 40°S. In order to compute the sea-to-air iodine flux  
33 supporting this chemistry, we compare previously established global sea surface iodide  
34 parameterisations with new, region-specific parameterisations based on the new iodide  
35 observations. This study shows that regional changes in salinity and sea surface temperature  
36 play a role in surface seawater iodide estimation. Sea-air fluxes of HOI and  $I_2$ , calculated from  
37 the atmospheric ozone and seawater iodide concentrations (observed and predicted), failed to  
38 adequately explain the detected IO in this region. This discrepancy highlights the need to  
39 measure direct fluxes of inorganic and organic iodine species in the marine environment.  
40 Amongst other potential drivers of reactive iodine chemistry investigated, chlorophyll-*a*  
41 showed a significant correlation with atmospheric IO ( $R = 0.7$  above the 99 % significance  
42 level) to the north of the polar front. This correlation might be indicative of a biogenic control  
43 on iodine sources in this region.

44

45 **Keywords:** iodine, Southern Ocean, Indian Ocean, marine boundary layer



46 **1. Introduction**

47 Iodine chemistry in the troposphere has gained interest over the last four decades after it was  
48 first discovered to cause depletion of tropospheric ozone ( $O_3$ ) (Chameides and Davis, 1980;  
49 Jenkin et al., 1985) and cause changes to the atmospheric oxidation capacity (Davis et al., 1996;  
50 Read et al., 2008). Iodine studies in the remote open ocean are important considering its role  
51 in tropospheric ozone destruction (Allan et al., 2000), the formation of potential cloud  
52 condensation nuclei and impact on cloud radiative properties (McFiggans, 2005; O'Dowd et  
53 al., 2002). However, iodine chemistry in the remote open ocean is still not completely  
54 understood, with uncertainties remaining around the sources and impacts of atmospheric iodine  
55 (Saiz-Lopez et al., 2012; Simpson et al., 2015).

56 Recent studies of atmospheric iodine chemistry have focused on the detection of iodine oxide  
57 (IO) in the marine boundary layer (MBL) as a fingerprint for active iodine chemistry. IO may  
58 itself also participate in particle nucleation if present at high concentrations (Saiz-Lopez et al.,  
59 2006b). Iodine containing precursor compounds undergo photo dissociation to produce iodine  
60 atoms (I), which rapidly react with ambient ozone, forming IO (Chameides and Davis, 1980).  
61 Until recently, fluxes of volatile organic iodine (e.g.  $CH_3I$ ,  $CH_2I$ ,  $CH_2I_2$ ) compounds  
62 including those originating from marine algae (Saiz-Lopez and Plane, 2004) were considered  
63 to be the primary source of iodine in the marine atmosphere (Carpenter, 2003; Vogt et al.,  
64 1999). However, the biogenic sources of atmospheric iodine could not account for the levels  
65 of IO detected in the tropical MBL (Mahajan et al., 2010b; Read et al., 2008). Currently,  
66 inorganic iodine emissions are considered to be the dominant sources contributing to the open  
67 ocean boundary layer iodine (Carpenter et al., 2013). A recent study by Koenig et al. (2020)  
68 concluded that inorganic iodine sources play major role in comparison to the organic iodine  
69 sources in contributing even to the upper troposphere iodine budget. Laboratory investigations  
70 revealed that at the ocean surface, iodide ( $I^-$ ) dissolved in the seawater reacts with the deposited



71 gas-phase ozone to release hypoiodous acid (HOI) and molecular iodine ( $I_2$ ) via the following  
72 reactions (Carpenter et al., 2013; Gálvez et al., 2016; MacDonald et al., 2014) :



77 The reaction of sea surface iodide (SSI) with ozone in (R1) is considered a major contributor  
78 (600-1000 Tg per year, (Ganzeveld et al., 2009)) to the loss of ozone at the surface ocean,  
79 contributing between 20 % (Garland et al., 1980) and 100 % (Chang et al., 2004) of the oceanic  
80 ozone dry deposition velocity. Reactions (R1) and (R2) result in the release of reactive iodine  
81 (HOI and  $I_2$ ) to the atmosphere, where they quickly photolyse to yield I atoms, which react  
82 with ozone in the gas phase to form IO (Carpenter, 2003; Saiz-Lopez et al., 2012). Carpenter  
83 et al. (2013) showed that the reactions (R1) and (R2) could account for about 75 % of the IO  
84 levels detected over the tropical Atlantic Ocean. Further studies have shown that including  
85 these reactions and the resulting fluxes of HOI and  $I_2$  in atmospheric chemistry models has  
86 results in good agreement between observed and modelled iodine levels over the Atlantic and  
87 the Pacific Ocean, but not for the Indian and Southern Ocean. For example, the sea-air flux of  
88 HOI and  $I_2$  could explain the observed levels of molecular iodine and IO at Cape Verde (Lawler  
89 et al., 2014b), and observed IO levels over the eastern Pacific were in reasonable agreement  
90 with those modelled from estimated  $I_2$  and HOI fluxes (MacDonald et al., 2014). In contrast,  
91 the inorganic iodine fluxes estimated for the Indian Ocean and Indian sector of the Southern  
92 Ocean marine boundary layer could not fully explain the observed IO concentrations (Mahajan  
93 et al., 2019a, 2019b).



94 Predicted global emissions of iodine compounds show a large sensitivity (~ 50 %) to the SSI  
95 field used (Saiz-Lopez et al., 2014; Sherwen et al., 2016a, 2016c); an improved and accurate  
96 system for simulating SSI concentration is imperative. Existing global parameterisations  
97 discussed in this study follow three different methods for SSI estimation. The first is a linear  
98 regression approach against biogeochemical and oceanographic variables (Chance et al.,  
99 2014), the second uses an exponential relationship with sea surface temperature as a proxy for  
100 SSI (MacDonald et al., 2014), and the third is a recent machine-learning-based model (Sherwen  
101 et al., 2019a) that predicts monthly global SSI fields for the present-day. Where such  
102 approaches are based on large scale relationships, they may not properly capture smaller scale,  
103 regional differences in SSI (as observed for Chance et al., 2014; MacDonald et al., 2014) or  
104 underestimate surface iodide concentration (in case of Sherwen et al., 2019). Furthermore, there  
105 are large differences in predicted iodide concentrations between these parameterisations in some  
106 regions (refer Sect. 3.2). Thus, estimation of seawater iodide based on the existing  
107 parameterisations may not always be sufficiently accurate.

108 At present, there is a paucity of measurements of SSI, and remote sensing techniques cannot  
109 detect iodine species in seawater (Chance et al., 2014; Sherwen et al., 2019a). In particular,  
110 regions of the Indian Ocean and the Southern Ocean have been under-sampled in terms of  
111 iodine observations in the atmosphere and ocean (Chance et al., 2014; Mahajan et al., 2019a,  
112 2019b). It is important to remember that the most widely used parameterisation (MacDonald  
113 et al., 2014) is built on a limited observational dataset from the Atlantic and Pacific Ocean  
114 completely excluding the Indian Ocean and the Southern Ocean. The parameterisations  
115 presented in Chance et al. (2014), are based on a larger data set including Southern Ocean  
116 observations, but still only make use of two data points in the Indian Ocean. Furthermore, the  
117 Sherwen et al. (2019) parameterisation uses the updated data set including the new Indian  
118 Ocean SSI observations used in this study. Compounding the lack of Indian Ocean SSI



119 observations is the fact that parts and in particular the Arabian Sea and the Bay of Bengal, do  
120 not follow the same seasonal trends in salinity (D'Addezio et al., 2015) and sea surface  
121 temperature (Dinesh Kumar et al., 2016) as each other on the same latitudinal band and hence  
122 the currently used global iodide parameterisations in models i.e. MacDonald et al. (2014) may  
123 not be appropriate for these areas. Here we use new SSI observations made as part of this study  
124 (described in full in Chance et al. (2019b) and included in Chance et al. (2019a)) to test whether  
125 the existing parameterisations can be directly applied to the Indian Ocean and if regional  
126 specific parameterisations are more accurate compared to the former.

127 Although several measurements of IO have been reported around the globe (Alicke et al., 1999;  
128 Allan et al., 2000; Frieß et al., 2001; Großmann et al., 2013; Mahajan et al., 2009, 2010a,  
129 2010b; Prados-Roman et al., 2015), the remote open ocean still remains under-sampled. The  
130 two documented observations of IO in the Indian Ocean and the Indian sector (Jan-Feb 2015  
131 and December 2015) of the Southern Ocean were interpreted using parameterisations to  
132 estimate the SSI concentrations in combination with observed ozone concentrations, to  
133 subsequently calculate the resulting inorganic iodine fluxes. This approach suggested that the  
134 observed atmospheric IO may not be well correlated with the inorganic fluxes and that biogenic  
135 fluxes could play an important role (Mahajan et al., 2019a, 2019b). Here, we present  
136 measurements of IO in the MBL of the Indian Ocean and the Southern Ocean during the 9<sup>th</sup>  
137 Indian Southern Ocean Expedition (ISOE-9) conducted in January-February 2017, alongside  
138 the first simultaneous SSI observations along the cruise track (Chance et al., 2019a). The iodide  
139 observations were used to compute the inorganic iodine fluxes to compare with IO observations  
140 along the cruise tracks. Further, observed SSI concentrations are used to compute region-  
141 specific parameterisations for SSI concentrations, following the approaches taken by Chance  
142 et al. (2014) and MacDonald et al. (2014). The iodide concentrations obtained with these  
143 region-specific modified parameterisations are compared to the iodide estimates using their



144 original counterparts and the global machine-learning-based prediction of SSI concentration  
145 (Sherwen et al., 2019a). The resulting estimated reactive iodine fluxes (HOI and I<sub>2</sub>) are then  
146 used to see if the inorganic fluxes can explain the IO loading in the atmospheric MBL.

## 147 **2. Measurement techniques and methodology**

148 The 9<sup>th</sup> Indian Southern Ocean Expedition (ISOE-9) was conducted from January to February  
149 2017 in the Southern Ocean and the Indian Ocean sector of the Southern Ocean. The expedition  
150 started from Port Louis, Mauritius, and spanned the remote open ocean area till the coast of  
151 Antarctica. Observations of IO, SSI and O<sub>3</sub> were made along the cruise track during ISOE-9.  
152 For further analysis we also include IO observations from the 2<sup>nd</sup> International Indian Ocean  
153 Expedition (IIOE-2) and the 8<sup>th</sup> Indian Southern Ocean Expedition (ISOE-8) conducted in the  
154 Indian and Southern Ocean region during austral summer of 2014-2015 (Mahajan et al., 2019a,  
155 2019b). We also include SSI observations in the northern Indian Ocean from two expeditions  
156 namely, the Sagar Kanya-333 cruise (SK-333) and the Bay of Bengal Boundary Layer  
157 Experiment (BoBBLE) conducted during June-July and September 2016 respectively (Chance  
158 et al., 2019b). Table 1 includes details of the expeditions, including the locations, dates of the  
159 expeditions and the meridional transect for each expedition. Figure 1a shows a map with the  
160 cruise tracks for the five expeditions. Figure 1b shows the seawater iodide sampling locations  
161 during ISOE-9, SK-333 and BoBBLE expeditions. The track of the ship during ISOE-9 along  
162 with the air mass back trajectories arriving at noon each day is given in the supplementary text  
163 Fig. S1. The HYbrid Single-Particle Lagrangian Integrated Trajectory (HYSPLIT) model  
164 (Rolph et al., 2017; Stein et al., 2015) was used to calculate the back trajectories. Similar back  
165 trajectory plots and full cruise tracks for ISOE-8 and IIOE-2 are given in Mahajan et al. (2019a,  
166 2019b). During the three expeditions, meteorological parameters of ocean and atmosphere were  
167 measured using an on-board automatic weather station and manual observation techniques.



168 **2.1. Sea surface iodide (SSI)**

169 In this section, we focus on developing region-specific parameterisation for SSI estimation by  
170 adapting previously established methods. The SSI concentrations obtained from the original  
171 and newly developed region-specific parameterisation and SSI model predictions are used for  
172 a comparison study, and further to calculate the inorganic iodine emissions.

173 **2.1.1 Observed SSI in the Indian Ocean and the Southern Ocean**

174 Historically, few observations of SSI are available for the Indian Ocean basin with reports of  
175 only 3 data points in the open ocean from the Arabian Sea sector of the Indian Ocean  
176 (Farrenkopf and Luther, 2002). Two of these values are coastal, and they lack supporting sea  
177 surface temperature and salinity data; thus, they have been excluded from this study. However,  
178 recent work has led to a large increase in the number of SSI observations available for the  
179 Indian Ocean and Southern Ocean (Indian ocean sector) (Chance et al., 2019b). Specifically,  
180 111 new observations were made during the 2016 ISOE-9 and 18 during the SK-333 and  
181 BoBBLE. During the ISOE-9, SSI measurements in seawater were made concomitant with  
182 observations of O<sub>3</sub> and IO in the gas phase for the first time. Observations of SSI made during  
183 this expedition used the cathodic stripping voltammetry method with a hanging mercury drop  
184 electrode as a working electrode (Campos, 1997; Luther et al., 1988). The seawater samples  
185 were collected during the ISOE-9 at a 3-6-hour interval between 23° S and 70° S. Seawater  
186 samples from the SK-333 cruise and BoBBLE were analysed following the same technique for  
187 surface iodide concentrations. Iodide data from SK-333 and BoBBLE contributed to 18  
188 additional data points between 10° N and 4° S making a total of 129 new locations (excluding  
189 coastal and extremely high values above 400 nM; see Chance et al. (2019b) for details) for  
190 observed SSI in the Indian Ocean and Southern Ocean region. This is a major sample size  
191 compared to the global 2014 database (n=925) across all the global oceans (Chance et al.,





192 2014), and these data points contribute substantially to the recently updated iodide dataset  
193 (Chance et al., 2019a) (n=1342). From here onwards, the iodide concentrations obtained from  
194 sampling observations will be referred to as measured SSI as opposed to modelled SSI to  
195 differentiate between the observed iodide concentrations and those calculated using the  
196 parametrisations. All available observations made in the Indian Ocean basin as presented in  
197 Chance et al. (2019a) have been included for the development of the region-specific  
198 parameterisation presented in this work. Further details about the measurement technique and  
199 the observations used can be found in Chance et al. (2019b).

#### 200 **2.1.2 Iodide parametrisations**

201 Due to the sparsity of SSI measurements, different empirical parametrisations have been  
202 proposed to estimate SSI concentrations. Parameters like SST and salinity (only for SK-333  
203 and BoBBLE;  $R^2 = 0.3$ ,  $P = 0.018$ ) show a positive correlation with the SSI concentrations.  
204 However, a global parameterisation scheme may not capture the specificities of these required  
205 for regional studies. The northern Indian Ocean has markedly different sea surface salinity  
206 (D'Addezio et al., 2015) and SST (Dinesh Kumar et al., 2016) in its two basins, the Arabian  
207 Sea and the Bay of Bengal, that share the same latitude bands separated by the Indian sub-  
208 continental landmass. These basins experience the biannually reversing monsoonal winds,  
209 which greatly influence their SST and salinity structure. Strong winds in the Arabian Sea  
210 associated with the summer monsoon dissipate heat via overturning and turbulent mixing.  
211 Whereas weaker winds in the Bay of Bengal imply high SST due to the formation of stable and  
212 shallow surface mixed layer (Shenoi, 2002). The Arabian Sea exhibits much higher salinity  
213 compared to the Bay of Bengal due to greater evaporation and lower river runoff (Rao and  
214 Sivakumar, 2003). Current global SSI parameterisations (MacDonald et al., 2014; Chance et  
215 al., 2014) are based almost entirely on observations from the Atlantic, Pacific and Southern  
216 (excluding the Indian ocean sector) Oceans, they may not be suitable for accurate estimation



217 of SSI in the distinct and highly variable salinity and temperature regimes of the Indian Ocean  
218 region.

219 Here, we aim to create region-specific parameterisations for the Indian and Southern Ocean  
220 and conduct a comparison between these and the existing global parameterisations, further  
221 discussed in Sect. 4.2. The existing global and the new region-specific parameterisations are  
222 listed in Table 2. Below we describe briefly the modified parameterisations. Details about the  
223 original parameterisations can be found in their respective publications (Chance et al., 2014;  
224 MacDonald et al., 2014; Sherwen et al., 2019a).

225 (a) Linear regression analysis was performed, on each parameter, namely, SST, mixed layer  
226 depth (MLD), latitude, sea surface nitrate concentration, and salinity against the measured SSI  
227 concentrations from ISOE-9, SK-333, and BoBBLE campaigns, similar to the Chance et al.  
228 (2014) technique, but using in situ SST and salinity observations instead of climatological  
229 values. More details on the approach taken can be found in the supplementary text. The  
230 combination with the largest  $R^2$  and uniform distribution of residuals from the statistically  
231 significant dependent variables, as detailed in Table S1 resulted in Eq. 2 of Table 2. Eq. 2 thus  
232 represents a region-specific (the Indian Ocean and the Southern Ocean region abbreviated as  
233 Ind. O. + Sou. O. in the figures) variant of the Chance et al. (2014) parameterisation for the  
234 estimation of SSI concentrations. Similarly, keeping in mind the difference in the SST and  
235 salinity for the Indian Ocean and the Southern Ocean, another parameterisation was derived  
236 only for the Southern Ocean region using the ISOE-9 iodide observations and for the Indian  
237 Ocean using the SK-333 and BoBBLE iodide observations, respectively. The parameterisation  
238 for the Southern Ocean region using ISOE-9 iodide observations is given in Table 2 as Eq. (3).  
239 A similar Indian Ocean parameterisation is not included in this text as the linear regression  
240 analysis fails to obtain a parametric equation for this region. This may be due to fewer data  
241 points ( $n=18$ ) combined for the Arabian Sea and Bay of Bengal basins.



242 (b) A second method for the estimation of SSI concentration was proposed by MacDonald et  
243 al. (2014) that uses the correlation between sea surface iodide and SST. At present, this is the  
244 most commonly used parameterisation in global models (Sherwen et al., 2016c, 2016b, 2016a;  
245 Stone et al., 2018). Similar to MacDonald et al. (MacDonald et al., 2014) (Table 2, Eq. 4), we  
246 derived an Arrhenius-type, region-specific expression using iodide and SST data from ISOE-  
247 9, SK-333 and BoBBLE. Figure 2 shows the typical linear dependence of  $\ln[I^-]$ , for observed  
248 SSI in the Indian Ocean and the Southern Ocean, with  $SST^{-1}$ , which resulted in the Arrhenius  
249 form expression given as Eq. (5) in Table 2.

250 Figure 3 shows the iodide concentrations for the three campaigns, ISOE-8, IIOE-2 and ISOE-  
251 9, calculated using equations (1) to (5), the measured iodide concentrations from ISOE-9, SK-  
252 333 and BoBBLE, and the global iodide model predictions obtained from Sherwen et al. (2019)  
253 (Table 2.). From here on, region-specific parameterisations developed for SSI concentrations  
254 are referred to as the modified versions of the original parameterisations; Eq. (2) and (3) are  
255 called the modified Chance et al. (2014) parameterisation for the Indian Ocean and Southern  
256 Ocean region and only the Southern Ocean region, respectively. Eq. (5) is called the modified  
257 Macdonald et al. (2014) parameterisation. The machine-learning-based model proposed in  
258 Sherwen et al. (2019) is referred to as ‘SSI model’ results.

## 259 **2.2. Ozone**

260 Surface ozone was monitored using a US-EPA approved nondispersive photometric UV  
261 analyser (Ecotech EC9810B) installed on the ship during the expeditions to detect surface  
262 ozone values at a one-minute temporal resolution. A Teflon tube ~ 4 m long fixed towards the  
263 front of the ship acted as an inlet for the analyser. The analyser is equipped with a selective  
264 ozone scrubber, which was alternatively switched in and out of the measuring stream. The  
265 analyser has a lower detection limit of 0.5 ppbv and a precision of 0.001 ppmv. A 5-micron



266 PTFE filter membrane installed in the sample inlet tube was changed regularly. Zero and span  
267 calibration were done every alternate day to ensure accurate  $O_3$  measurements. The ozone data  
268 collected was cleaned to remove the data points under the influence of the ship's smokestack  
269 by referring to the measured apparent wind direction on the ship. Apparent wind approaching  
270 the ship from 0 to 90° or 270 to 360° was considered free from smokestack emission influence,  
271 where 0 or 360° represents the bow of the ship. Ozone data recorded when the ship was  
272 stationary showed major smokestack emission influence and was excluded from the data.

### 273 **2.3. Estimation of inorganic iodine fluxes**

274 In order to estimate the contribution of inorganic iodine chemistry to active iodine chemistry  
275 in the atmosphere, the atmospheric fluxes for the main product species,  $I_2$  and HOI, need to be  
276 calculated, since direct flux measurements of  $I_2$  and HOI have not been done anywhere in the  
277 world to date. While there are reported observations of marine  $I_2$  emission, they are few in  
278 number and mostly from coastal regions (Atkinson et al., 2012; Huang et al., 2010; Saiz-Lopez  
279 et al., 2006a) and one observation in the open ocean (Lawler et al., 2014a), although these are  
280 all observations of atmospheric concentrations and not of fluxes. As observed SSI is not  
281 available for all cruises, we used the following scenarios for SSI to estimate the inorganic  
282 iodine fluxes:

283 (a) Using measured SSI: Observations of sea surface iodide from ISOE-9, SK-333, and  
284 BoBBLE.

285 (b) Using calculated SSI from:

286 1. Chance et al. (2014) parameterisation Eq. (1)

287 2. Modified Chance et al. (2014) parameterisation for the Indian Ocean and  
288 Southern Ocean (Ind. O. + Sou. O.) region Eq. (2)



- 289 3. Modified Chance et al. (2014) parameterisation for the Southern Ocean (Sou.  
290 O.) region Eq. (3)
- 291 4. MacDonald et al. (2014) parameterisation using SST Eq. (4)
- 292 5. Modified MacDonald et al. (2014) parameterisation Eq. (5)
- 293 6. Using machine learning SSI model predictions (Sherwen et al., 2019a) Eq. (6)

294 Ozone was measured on all three cruises (ISOE-9, IIOE-2 and ISOE-8). The fluxes for HOI  
295 and I<sub>2</sub> were then calculated for all the above scenarios except for the observations from SK-  
296 333 and BoBBLE as IO observations were not taken during these cruises. The following  
297 algorithm was used for estimating iodine fluxes (Carpenter et al., 2013),

$$298 \text{ flux}_{I_2} = [O_3(g)] * [I_{(aq)}^-]^{1.3} * (1.74 \times 10^9 - 6.54 \times 10^8 * \ln(ws)) \quad \text{Eq. (7)}$$

$$299 \text{ flux}_{HOI} = [O_3(g)] * \left( 4.15 \times 10^5 * \frac{\sqrt{[I_{(aq)}^-]}}{ws} - \frac{20.6}{ws} - 2.36 \times 10^4 * \sqrt{[I_{(aq)}^-]} \right) \text{Eq. (8)}$$

300 where, the fluxes are in nmol m<sup>-2</sup> d<sup>-1</sup>, [O<sub>3</sub>] in nmol mol<sup>-1</sup> (ppbv), [I<sup>-</sup>] in mol dm<sup>-3</sup> and the wind  
301 speed (WS) in m s<sup>-1</sup>. Carpenter et al. (2013) did not consider the effect of temperature in the  
302 interfacial layer of the sea-surface model on activation energies for the reaction R1 (i.e.,  
303 assumed the temperature dependence for k (I<sup>-</sup> + O<sub>3</sub>) to be zero). Although I<sub>2</sub> and HOI fluxes  
304 are expected to increase with the temperature of the interfacial layer, I<sub>2</sub> production has a  
305 negative activation energy, as noted by MacDonald et al. (2014). In Carpenter et al. (2013)  
306 (specific to the tropical Atlantic), a seawater temperature of 15°C and air temperature of 20°C  
307 were used to calculate Henry's law constants, diffusion constants, and mass transfer velocities.  
308 Again assuming the temperature dependence of k(I<sup>-</sup> + O<sub>3</sub>) to be zero, but including the  
309 temperature-dependence of Henry's law constants, diffusion constants, and mass transfer  
310 velocities, the same interfacial layer model predicted effective activation energies for I<sub>2</sub> and  
311 HOI emissions of -2 kJ mol<sup>-1</sup> and 25 kJ mol<sup>-1</sup> (Macdonald et al. (2014). Using these



312 activation energies, Macdonald et al. (2014) calculated differences in I<sub>2</sub> and HOI fluxes of 3 %  
313 and 31-41 %, respectively, at SSTs of 10° C and 30° C compared to the room-temperature  
314 parameterisations presented in Carpenter et al. (2013). Experimentally derived activation  
315 energies for I<sub>2</sub> and HOI emissions were  $-7 \pm 18$  kJ mol<sup>-1</sup> and  $17 \pm 50$  kJ mol<sup>-1</sup> (MacDonald  
316 et al., 2014). As HOI represents the larger iodine flux, the higher relative uncertainty in the  
317 activation energy should be kept in mind when calculating temperature-dependent emissions.

318 HOI and I<sub>2</sub> fluxes are also influenced by the wind speed as seen from equations (7) and (8),  
319 and the modelled iodine fluxes (HOI and I<sub>2</sub>) are highest for high [O<sub>3</sub>], high [I] and low wind  
320 speed. This is explained by the assumption that wind shear drives mixing of the interfacial layer  
321 to bulk seawater, reducing the efflux of HOI and I<sub>2</sub> into the atmosphere (Carpenter et al., 2013).  
322 Negative fluxes are obtained from equations (7) and (8) for both HOI and I<sub>2</sub> when the wind  
323 speed is higher than 14 m s<sup>-1</sup>, which is not physically possible and therefore the model output  
324 is limited to wind speeds below 14 ms<sup>-1</sup> (Mahajan et al., 2019a). Iodine fluxes calculated from  
325 equations (7) and (8) using SSI concentrations from the scenarios (a) and (b 1-6) are shown in  
326 Fig. 4 (c and d).

## 327 **2.4. Iodine Oxide**

### 328 **2.4.1 Observations**

329 Ship-based measurements of IO were made using the Multi-Axis Differential Optical  
330 Absorption Spectroscopy (MAX-DOAS) technique (Hönninger et al., 2004; Platt and Stutz,  
331 2008). The MAX-DOAS was installed at the bow of the ship with a direct line of sight towards  
332 the front of the ship to avoid the ship's plume in the detection path of the telescope. The MAX-  
333 DOAS was programmed to capture scattered sunlight spectra at every 1 second at set elevation  
334 angles of 0, 1, 2, 3, 5, 7, 20, 40, and 90-degrees during daylight hours. Mercury line calibration  
335 offset, and dark current spectra were recorded after sunset on each day. Elevation angles



336 outside a range of  $\pm 0.2$  degree from the set value were eliminated from the 30 minutes averaged  
337 spectra for increased accuracy. Figure S2 shows the resultant IO and O<sub>4</sub> differential slant  
338 column densities (DSCDs) for ISOE-9 campaign, similar plots are available for ISOE-8  
339 (Mahajan et al., 2019a) and IIOE-2 (Mahajan et al., 2019b). The QDOAS software (Danckaert  
340 et al., 2017) was used for DOAS retrieval of IO from the spectra using the optical density fitting  
341 analysis method. The spectra were fitted with a 3<sup>rd</sup> order polynomial using fitting interval of  
342 415 to 440 nm with cross-sections of NO<sub>2</sub> (Vandaele et al., 1998), O<sub>3</sub> (Bogumil et al., 2003),  
343 O<sub>4</sub> (Thalman and Volkamer, 2013), H<sub>2</sub>O (Rothman et al., 2013), two ring spectra, first as  
344 recommended by Chance and Spurr, (1997) and second following Wagner et al., (2009) and a  
345 liquid water spectrum for seawater (Pope and Fry, 1997). To remove the influence of  
346 stratospheric absorption a spectrum corresponding to 90° (zenith) from each scan was used as  
347 a reference for the analysis. The raw spectra were analysed to obtain differential slant column  
348 densities (DSCDs), and values with a root mean square error (RMS) of greater than 10<sup>-3</sup> were  
349 eliminated. Similarly, DOAS retrieval of O<sub>4</sub> in 350 to 386 nm spectral window was performed,  
350 and DSCDs were obtained. The optical density fits for IO and O<sub>4</sub> from ISOE-9 are shown in  
351 Fig. S3. The IO DSCDs were then converted to volume mixing ratios using the O<sub>4</sub> slant  
352 columns following the previously used "O<sub>4</sub> method" (Mahajan et al., 2012; Prados-Roman et  
353 al., 2015; Sinreich et al., 2010; Wagner et al., 2004). Further details of the instrument, retrieval  
354 procedure and conversion into mixing ratios can be found in previous works (Mahajan et al.,  
355 2019a, 2019b).

#### 356 **2.4.2 Modelled atmospheric IO**

357 We use outputs from two global models for a comparison with the observations conducted  
358 during the three cruises. The first model is the GEOS-Chem chemical transport model (version  
359 10-01, 4x5 degrees horizontal resolution, <http://www.geos-chem.org>), which includes detailed  
360 HO<sub>x</sub>-NO<sub>x</sub>-VOC-ozone-halogen-aerosol tropospheric chemistry (Sherwen et al., 2016c, 2017)



361 and is driven by offline meteorology from NASA's Global Modelling and Assimilation Office  
362 (<http://gmao.gsfc.nasa.gov>) forward processing product (GEOS-FP).

363 The second model is the 3D chemistry-climate model CAM-Chem version 4 (Community  
364 Atmospheric Model with Chemistry) (<https://www2.acom.ucar.edu/gcm/cam-chem>), which is  
365 included in the CESM framework (Community Earth System Model, CAM-Chem, version  
366 4.0). The model includes a state-of-the-art halogen chemistry scheme (chlorine, bromine and  
367 iodine) (Saiz-Lopez and Fernandez, 2016). The current configuration includes an explicit  
368 scheme of organic and inorganic iodine emissions and photochemistry. These halogen sources  
369 comprise the photochemical breakdown of five very short-lived bromocarbons ( $\text{CHBr}_3$ ,  
370  $\text{CH}_2\text{Br}_2$ ,  $\text{CH}_2\text{BrCl}$ ,  $\text{CHBrCl}_2$  and  $\text{CHBr}_2\text{Cl}$ ) naturally emitted by phytoplankton from the  
371 oceans (Ordóñez et al., 2012). The model was run in specified dynamic mode (Ordóñez et al.,  
372 2012), with a spatial resolution of  $1.9^\circ$  latitude by  $2.5^\circ$  longitude and 26 vertical levels from the  
373 surface to up to 40 km.

374 Both models include biotic emissions of four iodocarbons ( $\text{CH}_3\text{I}$ ,  $\text{CH}_2\text{ICl}$ ,  $\text{CH}_2\text{IBr}$  and  $\text{CH}_2\text{I}_2$ )  
375 as described by (Ordóñez et al., 2012) and abiotic oceanic sources of HOI and  $\text{I}_2$  based on the  
376 Carpenter et al. (2013) and MacDonald et al. (2014) laboratory studies of the oxidation of  
377 aqueous iodide by atmospheric ozone at the ocean surface. Both models here use the  
378 MacDonald parameterisation expression (Eq. (4), MacDonald et al., 2014) discussed in Section  
379 2.1.2 to predict surface iodide used for calculating iodine emissions and the organo-halogen  
380 emissions from Ordoñez et al. (2012). IO surface concentrations for the three campaigns (IIOE-  
381 2, ISOE-8 and ISOE-9) were extracted from the model runs and used for comparison.  
382 Currently, these two global models include reactive iodine chemistry (along with TOMCAT,  
383 which includes the tropospheric iodine chemistry (Hossaini et al., 2016)).

### 384 **3. Results**





### 385 **3.1 Ozone, Meteorological and Oceanic parameters**

386 The latitudinal distribution of hourly average values of wind speed (WS), O<sub>3</sub>, SST, and salinity  
387 from all the campaigns are shown in Fig. 5. Winds arriving at the ship, shown in the first panel  
388 (Fig. 5a), remained low for most of the duration of all three expeditions with wind speed  
389 ranging from 1 m s<sup>-1</sup> to stronger winds of 24 m s<sup>-1</sup> on a few days. Even stronger winds (above  
390 30 m s<sup>-1</sup>) were observed during the ISOE-9 in the region between 64° and 65° S with the highest  
391 wind speed of 32 m s<sup>-1</sup> at 66° S on the night of 8<sup>th</sup> February 2017. Ozone mixing ratios, (Fig.  
392 5b) during all three expeditions showed a similar trend exhibiting a large reduction in values  
393 in the open ocean environment compared to coastal environments. The back trajectories  
394 (supplementary text) show that for most of the expeditions, air masses arriving at the cruise  
395 were from the open ocean environment and did not have any anthropogenic influence for the  
396 last five days. This is reflected in the O<sub>3</sub> values, which range between 8 and 20 ppbv in the  
397 open ocean but were between 30 and 50 ppbv near the coastal regions, where the air mass back  
398 trajectories confirm anthropogenic origins. Close to the Indian sub-continent ozone levels  
399 peaked at about 50 ppbv during the ISOE-8. It also showed a distinct diurnal variation with  
400 higher ozone values during the daytime due to photochemical production. However, in the open  
401 ocean environment, ozone mixing ratios did not show this diurnal variation, and indeed values  
402 of ozone dropped during daytime indicating photochemical destruction during both ISOE-8  
403 and ISOE-9 (Fig. 5b).

404 As already noted, SST is widely used to predict SSI (Eq. 4 and 5). Combined SST data (Fig.  
405 5c) reveal a steady decrease in sea surface temperature from 15° S to 68° S for all the  
406 campaigns. During January 2015 (ISOE-8) seawater north of 6° N displays slightly lower SST  
407 (~ 3° C) compared to that in December 2015 (IIOE-2). Salinity is also an important parameter  
408 for the prediction of SSI (higher coefficient in Eq. 1, 2 and 3). The Southern Ocean region  
409 explored during ISOE-8 and ISOE-9 reveals similar salinity values (Fig. 5d) for the austral



410 summer months of 2014 and 2016 (January-February). The salinity data shows relatively lower  
411 values for ISOE-8 compared to those for IIOE-2 for the region 15° N to 20° S. Despite the inter-  
412 annual differences in the northern Indian Ocean region, salinity values of ~ 35 PSU overlap for  
413 the IIOE-2 and ISOE-8 in a small window of 7° N to the equator. Below the equator, the salinity  
414 values for IIOE-2 increase while for ISOE-8 salinity remains lower than 35 PSU until 20° S.  
415 Seawater between 20° S and 44° S has a near-constant salinity of 35 PSU which decreases to  
416 ~33.5 PSU after 44° S and remains the same until 65° S after which the salinity begins to drop  
417 to 31.5 PSU near 67° S close to Antarctica.

### 418 **3.2 Sea surface iodide concentration**

419 Latitudinal averages of SSI concentrations estimated from seven scenarios (listed in Sect. 2.3)  
420 are shown in Fig. 3. SSI estimates from the IIOE-2 campaign are marked separately to  
421 differentiate from the ISOE estimates for the Indian Ocean region. There is a clear difference  
422 in the estimated SSI in different scenarios. All the estimates and the model follow a similar  
423 pattern showing elevated levels in the tropics as compared to the higher latitudes. SSI estimates  
424 from parameterisations (Eq. 1, 3, 4, and 5) show nearly constant values for SSI from 15° N to  
425 25° S, after which a steady decline is noted until 70° S. Thus, the parameterisations based on Eq.  
426 1, 3, 4 and 5 do not capture the decreasing trend observed for iodide around the equator. Eq. 2,  
427 which was derived specifically for the Indian Ocean and Southern Ocean region better captures  
428 this trend, and also shows a better match with the measured SSI from SK-333 and BoBBLE in  
429 the Indian Ocean. Eqn. 6 also predicts lower concentrations around the equator than in the  
430 northern Indian Ocean. SSI concentrations estimated using the Chance et al. (2014)  
431 parameterisation (Eq. 1) show a small increase in iodide concentrations south of 47° S (polar  
432 front), which is not observed in the other parameterisations, but there is some suggestion of in  
433 the observations. Eq. 1 also resulted in a large difference (~ 50 nM) of SSI estimates north of  
434 10° N between the IIOE-2 and ISOE-8 cruises; while this difference was lower for the other



435 parameterisations. This difference between the SSI estimates for the IIOE-2 and ISOE-8 cruises  
436 is due to the large difference in salinity values for this region (Sect. 4.1). SSI estimates using  
437 Eq. 2 shows good agreement with the model prediction of Sherwen et al. (2019), both  
438 indicating a decrease in SSI concentrations near the equator during the IIOE-2 and ISOE-8  
439 expeditions. Some high SSI concentrations (up to ~250 nM) were observed around 10° N, these  
440 were best replicated by Eqn.3. The highest SSI concentrations estimated using Eq. 3 were 244  
441 nM at 7° N during IIOE-2 and 242 nM at 12° S during ISOE-8. At the equator, Eq. 2 performs  
442 better in predicting the SSI concentrations with a difference of ~75 nM compared to the  
443 observations. SSI estimates from Eq. 4, i.e. MacDonald et al. (2014) parameterisation, were  
444 lower than the measured iodide concentrations and all other parameterisation, including the  
445 model (Eq. 7) predictions. Overall, all modified parameterisations (Eq. 2, 3 and 5) estimate  
446 higher SSI compared to the original parameterisation (Eq. 1 and 4), with the exception of the  
447 region south of 20° S, where Eq. 3 predicts lower SSI than Eq. 1. The modified MacDonald  
448 parameterisation (Eq. 5) estimated iodide concentrations to be greater by 50 nM for the entire  
449 dataset in comparison to the existing MacDonald parameterisation given by Eq. 4. For Eq. 5,  
450 the uncertainty in the iodide concentration from the 95 % prediction band is ~15 % of the  
451 predicted value.

### 452 3.3 Iodine fluxes

453 Figure 4 shows the latitudinal variation in IO mixing ratios, inorganic iodine emissions (HOI  
454 and I<sub>2</sub>), chl-*a* and ozone mixing ratios for the entire dataset comprising of the three campaigns.  
455 All the panels in Fig. 4 are plots of daily averaged values during each expedition, except for  
456 the HOI and I<sub>2</sub> fluxes; these are latitudinal averages from each campaign. Emissions calculated  
457 using the measured SSI concentrations (represented by filled spheres in Fig. 4 c & d) from  
458 ISOE-9 correspond to the data points of the measured SSI concentration. Oceanic inorganic  
459 iodine emission fluxes of HOI and I<sub>2</sub> were estimated using the Carpenter et al. (2013)



460 parameterisation given in Eq. (7) and (8) limited to wind speeds below  $14 \text{ m s}^{-1}$ . Thus, the  
461 fluxes estimated from the measured SSI concentrations were reduced to 56 points (out of 111  
462 measured SSI data points). The seven different datasets of iodide concentrations (listed in Sect.  
463 2.3) have been used for estimation of HOI and  $\text{I}_2$  fluxes. For the entire dataset, the highest  
464 fluxes were obtained when using the SSI concentrations from the modified Chance et al. (2014)  
465 parameterisation (Eq. 3), derived from measured SSI from the Southern Ocean region, i.e.  
466 during ISOE-9. The second highest fluxes were estimated using SSI from Eq. 2, obtained from  
467 measured SSI from the Indian Ocean and Southern Ocean. Comparatively lower iodine  
468 emissions were estimated using SSI concentration from MacDonald et al. (2014)  
469 parameterisation (Eq. 4). The estimated inorganic iodine fluxes in the Southern Ocean region  
470 ( $30^\circ \text{ S}$  and below) are much lower compared to the Indian Ocean (Fig. 5), driven by the higher  
471 estimated SSI in the latter. Maximum inorganic emissions are predicted in the tropical region,  
472 specifically, north of the equator. HOI is the dominant reactive iodine precursor species for the  
473 entire dataset, with calculated flux values 20 times higher than those for  $\text{I}_2$ . Emissions estimated  
474 using SSI from Eq. (3), resulted in a peak HOI flux of  $1.5 \times 10^9 \text{ molecules cm}^{-2} \text{ s}^{-1}$  at  $9^\circ \text{ N}$  during  
475 ISOE-8. The lowest HOI flux of  $1.7 \times 10^6 \text{ molecules cm}^{-2} \text{ s}^{-1}$  was obtained at  $61^\circ \text{ S}$  during ISOE-  
476 9. For the same latitudes ( $9^\circ \text{ N}$  and  $61^\circ \text{ S}$ ), a maximum  $\text{I}_2$  flux of  $7.0 \times 10^7 \text{ molecules cm}^{-2} \text{ s}^{-1}$   
477 and a minimum of  $1.3 \times 10^5 \text{ molecules cm}^{-2} \text{ s}^{-1}$  were estimated, respectively. Flux estimates from  
478 Eq. 2 are slightly lower, with a maximum HOI flux of  $1.3 \times 10^9$  and a minimum of  $5.8 \times 10^5$   
479  $\text{molecules cm}^{-2} \text{ s}^{-1}$  and maximum  $\text{I}_2$  flux of  $5.2 \times 10^7$  with minimum of  $8.3 \times 10^4 \text{ molecules cm}^{-2}$   
480  $\text{s}^{-1}$  at the same latitudes. The estimated HOI and  $\text{I}_2$  emissions are notably lower (by  $\sim 50 \%$ )  
481 during IIOE-2 to the north of  $5^\circ \text{ S}$  compared to emissions from ISOE-8. Between  $5^\circ \text{ S}$  and  $20^\circ$   
482  $\text{S}$ , the emissions from IIOE-2 and ISOE-8 are similar. Fluxes estimated using measured SSI  
483 concentrations for the ISOE-9 campaign ( $20^\circ \text{ S}$  to  $70^\circ \text{ S}$ ) show no strong latitudinal trend for  
484 both HOI and  $\text{I}_2$  emissions. The maximum calculated HOI flux was  $5.8 \times 10^8 \text{ molecules cm}^{-2} \text{ s}^{-1}$



485 <sup>1</sup> at 68° S and the minimum was  $1.1 \times 10^7$  molecules  $\text{cm}^{-2} \text{s}^{-1}$  at 33° S. Similarly,  $\text{I}_2$  fluxes  
486 estimated from measured SSI concentrations peaked at  $1.5 \times 10^7$  molecules  $\text{cm}^{-2} \text{s}^{-1}$  at 32° S with  
487 a minimum of  $3.5 \times 10^5$  molecules  $\text{cm}^{-2} \text{s}^{-1}$  at 67° S. Inorganic iodine emissions estimated using  
488 model predictions for SSI concentrations from Sherwen et al. (2019) match well with the fluxes  
489 estimated using the iodide parametrisation tools. Despite the differences in SSI concentrations  
490 from existing and region-specific parameterisations, all result in similar values for iodine fluxes  
491 and so SSI cannot explain discrepancies in the observed and modelled IO levels in this region.

### 492 **3.4 Iodine oxide**

#### 493 **3.4.1 Observations**

494 IO was detected above the instrument detection limit ( $2.1 - 3.5 \times 10^{13}$  molec.  $\text{cm}^{-2}$  i.e. 0.4 – 0.7  
495 pptv) in all three campaigns. The expeditions covered a track from the Indian Ocean to the  
496 Antarctic coast in the Southern Ocean and showed lower IO DSCDs in the tropics compared  
497 to the Southern Ocean, with a peak of about  $3 \times 10^{13}$  molec.  $\text{cm}^{-2}$  at 40° S. Figure 4a shows  
498 daily averaged IO mixing ratios for all the three cruises combined. IO mixing ratios of up to 1  
499 pptv were observed in the region 50° - 55° S and slightly higher values of IO mixing ratios were  
500 observed in the region below 65° S close to the Antarctic coast. North of the polar front region,  
501 the maximum IO average mixing ratio of ~1 pptv was observed at 40° S. The highest values of  
502 IO were observed close to the Antarctic coast, with up to 1.5 pptv measured during ISOE-9  
503 and similar values are reported for the ISOE-8 expedition south of the polar front (Mahajan et  
504 al., 2019a). The IO mixing ratios in the Southern Ocean region for ISOE-9 ranged between 0.1  
505 and a maximum of  $1.57 (\pm 0.37)$  pptv observed on 18 Feb 2017 at 50° S on a clear sky day.  
506 This maximum value was observed only on one day, and preceded by foggy and misty days,  
507 later followed by overcast for several days evidencing the role of photochemistry in IO  
508 production from its precursor gases.



### 509 **3.4.2 Modelled IO**

510 Based on the current understanding of iodine chemistry, regional and global models consider  
511 inorganic fluxes of iodine (HOI and I<sub>2</sub>) as major contributors of iodine in the marine boundary  
512 layer. It is important to verify if the models using the existing parameterisation for these source  
513 gases can replicate observations of IO in the region of study. Thus, we have included model IO  
514 output from GEOS-Chem and CAM-Chem, both of which use the SST based MacDonald et  
515 al. (2014) parameterisation for SSI (Fig. 4b). The surface IO output from GEOS-Chem predicts  
516 the highest levels of IO up to 1.7 pptv to the north of the equator at 11° N for the time period  
517 of the IIOE-2 campaign. For the same latitudes, the model suggests lower IO levels, of less  
518 than 0.5 pptv, during the ISOE-8 campaign. Conversely, south of the equator to 10° S, the  
519 model predicts higher IO levels during the ISOE-8 and lower IO values during the IIOE-2, in  
520 agreement with the observations. Below 10° S, IO predictions for both campaigns match well  
521 until 20° S, which was the latitudinal limit for the IIOE-2 campaign. To the south of 20° S,  
522 modelled IO levels remained below 1 pptv and exhibited a decreasing trend to the south of the  
523 polar front, in disagreement with IO observations. At locations between 40° S and 43° S,  
524 GEOS-Chem underestimates the observed IO levels by 50 %. These locations are close to the  
525 Kerguelen Islands, and high IO values were observed here only during the ISOE-8. These  
526 locations have been omitted in the correlation study between modelled and observed IO as they  
527 could be impacted by coastal or upwelling emissions, which are not well prescribed in the  
528 models.

529 The CAM-Chem IO surface output suggests consistently higher levels of IO during IIOE-2  
530 compared to the ISOE-8 for the same latitudinal band (Fig. 4b). Contrary to the observations,  
531 the CAM-Chem model suggests that IO levels during the IIOE-2 are up to 1 pptv higher than  
532 the ISOE-8 campaign near 7° S latitude. The model also shows elevated IO levels of 2.7 pptv  
533 at 7.9° N during the IIOE-2 campaign, which does not match the observations during the IIOE-



534 2 or the ISOE-8 for that region. IO levels below 1.5 pptv (11° N to 20° S) are indicated for the  
535 ISOE-8 campaign. In addition, the region between 0° and 1.5° S has similar IO levels for the  
536 IIOE-2 and ISOE-8 campaigns. The model predicts lower IO levels for the south Indian Ocean  
537 and the Southern Ocean (less than 1 pptv) with decreasing IO to the south of the polar front.  
538 However, at 43° S, the model suggests higher IO (2.4 pptv) during the ISOE-9, which matches  
539 the increase in observed IO for that region during the ISOE-8 expedition, with this region being  
540 close to the Kerguelen Islands Both models show consistently higher absolute concentrations  
541 overall compared to the observations north of the polar front.

## 542 **4. Discussion**

### 543 **4.1 Seawater iodide**

544 To improve the estimation of SSI in the study region, previously established parameterisations  
545 (Eq. 1 and 4) were modified to obtain a region-specific parameterisation for SSI concentrations.  
546 SSI estimated using these modified parameterisations were less sensitive to seasonal salinity  
547 and SST changes for the north Indian Ocean basin compared to the existing parameterisation  
548 (Fig 3). Figure 6 shows the correlations of all the calculated SSI concentrations with the  
549 observations. The SSI estimates from Eq. 1 to 6 correlate positively (significantly) to the  
550 measured SSI concentrations (observations) from ISOE-9 (Fig. 6). Out of the six  
551 parameterisation tools compared in this study, as expected, SSI from Eq. (2) i.e. the modified  
552 Chance equations for the Indian Ocean and the Southern Ocean showed the best correlation  
553 with the measured SSI because they were created using datasets from these campaigns (Fig. 6  
554 and Table 2). Although the region-specific parameterisations were expected to match with the  
555 observations they are based on, there was a notable difference between predictions and  
556 observations when this approach was applied only to Indian Ocean SSI measurements from  
557 SK-333 and BoBBLE ( $R^2 = 0.5$  for Indian Ocean parameterisation, analysis not shown). This



558 could be attributed to the lack of SSI measurements in this region ( $n=18$ ), and it highlights the  
559 fact that there may be not only seasonally but regionally varying complexities in SSI which  
560 should be considered when estimating SSI. All parameterisation methods used for SSI  
561 estimations show that SSI concentrations are directly proportional to seawater salinity (listed  
562 in Sect. 2.3). It is evident from Fig. 5d and Fig. 3a that to the north of the equator, the  
563 parameterisations (Eq. 1 to 5) show lower SSI concentrations in regions with lower salinity (up  
564 to  $5^{\circ}$  N during ISOE-8 – filled symbols Fig. 3) and higher SSI concentrations in regions with  
565 comparatively higher salinity (during IIOE-2 – unfilled symbols Fig. 3). Only the modelled  
566 SSI concentrations using Eq. 6 (Fig. 3a, data in purple) reveal an inversely proportional  
567 relationship for salinity and SSI concentration in this region. The Sherwen et al. (2019)  
568 parametrisation (Eq. 6) produces lower SSI concentrations in high salinity Arabian Sea waters  
569 during IIOE-2 (Fig. 3a) north of  $5^{\circ}$  N, compared to the low salinity Bay of Bengal waters during  
570 ISOE-8 which contradicts all the other parameterisation (Eq. 1 to 5). Further, the SSI  
571 concentrations obtained from Sherwen et al. (2019) reverse their trend to the south of  $6^{\circ}$  N,  
572 with higher concentrations during IIOE-2 and lower during ISOE-8. It should be noted that  
573 only a few observations of SSI exist in this region to confirm this trend. Further discussion on  
574 the relationship between salinity and other biogeochemical variables with SSI concentrations  
575 at a global and regional scale can be found elsewhere (Chance et al., 2014, 2019a).

576 SSI estimates considering only SST as a proxy for iodide concentration (Eq. 4), reveal positive  
577 correlations with measured SSI concentration ( $R = 0.86$ ,  $P < 0.001$ ,  $n = 129$ ; Fig. 6d). The  
578 modified MacDonald parameterisation (Eq. 5) also correlates positively to the measured SSI  
579 concentration but has a slightly lower coefficient of correlation ( $R = 0.83$ ,  $P < 0.001$ ,  $n = 129$ ;  
580 Fig. 6e). When using the SST as a proxy for SSI, a large intercept was obtained for the SSI  
581 values, evidencing the discrepancy in absolute value between this parametrisation and the  
582 observations. Eq. (5) resulted in a lower intercept, approximately half of that for Eq. (4), and a





583 lower absolute slope value of  $|-3763\pm 218|$  compared to the  $|-9134\pm 613|$  of Eq. (4) given in  
584 MacDonald et al. (2014). The lower absolute slope value for Eq. (5) implies that the SSI  
585 concentrations for this region were less sensitive to the changes in SST compared to that in Eq.  
586 (4).

587 Despite the lower R-value, the SSI estimates from Eq. 5 in Fig. 3 are closer to the measured  
588 SSI concentration than the estimates from Eq. 2 and 3 for the region from 25° S to 70° S.  
589 However, north of 25° S, the SSI estimates from Eq. 3 and Eq. 5 differ by ~40 %. Both SST  
590 based parameterisation (Eq. 4 and 5) did not show the observed latitudinal variation in the SSI  
591 concentrations near the equator. Linear regression of SSI with SST for only the Indian Ocean  
592 region revealed that there was no correlation between the two ( $R^2 = 0.07$ ,  $P = 0.3$ ,  $n = 18$ ). The  
593 SSI in this region only showed dependence on the salinity and latitude, correlations with the  
594 other parameters were not significant. This highlights that SST may not be a very good proxy  
595 for SSI in the Indian Ocean, especially near the equator. This is explored further in Chance et  
596 al. (2019b). The original Chance et al. (2014) parameterisation displays higher sensitivity to  
597 seasonal salinity changes compared to the existing and modified parameterisation in the Indian  
598 Ocean region (Sect. 3.3). However, this method predicted increasing iodide concentration to  
599 the south of the polar front (47° S), which is not supported by observations in this region (Fig.  
600 3). In conclusion, considering the correlation with measured SSI concentration and dependence  
601 on seawater salinity, the region-specific modified Chance parameterisation (Eq. 2) is a suitable  
602 method to estimate SSI concentration for the Indian Ocean and Southern Ocean region. The  
603 modelled SSI estimates by Sherwen et al. (2019) capture SSI trend close to equator better than  
604 other existing schemes but it fails to replicate higher SSI observations at locations 8° N, 40° S  
605 and to the south of 65° S close to the Antarctic coast (Fig. 3).

#### 606 **4.2 Atmospheric iodine**



607 Combined IO observations from IIOE-2, ISOE-8, and ISOE-9 (Fig. 4a) show that the Indian  
608 Ocean region has comparatively less IO in its MBL than the Southern Ocean region. IO  
609 remained below 1 pptv up to 40° S and reached a maximum IO of 1.6 pptv south of the polar  
610 front. Modelled surface IO output from GEOS-Chem and from CAM-Chem using the  
611 Macdonald et al. (2014) parameterisation (Fig. 4b) do not match the observations of IO,  
612 although they generally show good agreement with each other. The models show similar spatial  
613 patterns across the entire dataset, except for two periods of very high IO levels predicted by  
614 CAM-Chem (Fig. 4b). As well as structural differences between CAM-Chem and GEOS-  
615 Chem, there are many halogen specific differences in rate constants, heterogeneous  
616 parameters, cross-sections and photolysis of species (e.g. higher iodine oxides) which could  
617 explain differences in predicted gas-phase IO. Considering the generally lower wind speeds  
618 and higher ozone concentrations seen in IIOE-2 versus SOE-8 and SOE-9, the calculated fluxes  
619 are higher and therefore more sensitive to assumptions, such as minimum wind speeds provided  
620 to the Carpenter et al. (2013) parameterisation. GEOS-Chem uses a minimum wind speed of  
621 5 m s<sup>-1</sup>; however, CAM-Chem uses a minimum wind speed of 3 m s<sup>-1</sup>.

622 Both models suggest higher than observed IO levels in the Indian Ocean region but under-  
623 predict IO for the Southern Ocean region. The highest detected IO levels, both in the Southern  
624 Ocean and in a narrow band around 43° S, were not reflected in the model predictions. We note  
625 these occurred in regions of elevated chl-*a* values (Fig. 5), and that Mahajan et al. (2019a) also  
626 reported positive correlations for IO with chl-*a* for the Indian Ocean region, above the polar  
627 front for a subset of the dataset (ISOE-8). Calculated fluxes of HOI and I<sub>2</sub> (Fig. 4c and d) fail  
628 to directly explain trends in the detected IO levels for the entire dataset, regardless of the  
629 method used to estimate SSI. Maximum levels of HOI and I<sub>2</sub> predicted to the north of 5° N  
630 correspond to rather low levels of IO (< 0.5 pptv) in this region. However, this has been  
631 attributed to NO<sub>x</sub> titration of IO (Mahajan et al., 2019b). The models, however, do not capture



632 this iodine titration by  $\text{NO}_x$  as seen in the observations; even though the reactions of IO with  
633  $\text{NO}_x$  are included (Ordóñez et al., 2012). Similarly, for the region south of the polar front, the  
634 calculated iodine fluxes remain low in the region of the maximum detected IO concentrations  
635 during the ISOE-8 and ISOE-9 campaigns. Iodine fluxes estimated for the Indian Ocean region  
636 ( $15^\circ \text{N}$  to  $5^\circ \text{N}$ ) during IIOE-2 and ISOE-8 show large differences with much higher values  
637 during ISOE-8. However, the modelled IO is in fact higher for IIOE-2 than during ISOE-8 ( $5^\circ$ -  
638  $15^\circ \text{N}$ ). Considering that the models do not reflect the fluxes, this indicates that photochemistry  
639 led to this difference in the model. Additionally, the elevated levels of IO predicted in the  
640 models suggest that CAM-Chem and GEOS-Chem overestimate the impact of iodine chemistry  
641 in the northern Indian Ocean.

642 In Fig. 7, correlations of iodine fluxes estimated using the measured SSI concentrations (Eq.  
643 2) show that fluxes of HOI correlate positively with tropospheric ozone ( $R = 0.56$ ,  $P < 0.001$ )  
644 and negatively to wind speed ( $R = -0.62$ ,  $P < 0.001$ ) and  $\text{I}_2$  fluxes correlate positively with SSI  
645 concentration ( $R = 0.56$ ,  $P = P < 0.001$ ) and ozone ( $R = 0.59$ ,  $P < 0.001$ ) and negatively to wind  
646 speed ( $R = -0.4$ ,  $P < 0.001$ ). This indicates that although there is positive correlation of  $\text{I}_2$  with  
647 SSI, the dominant inorganic iodine flux i.e. HOI does not show significant correlation with SSI  
648 concentration, although the flux equation includes an iodide term (Eq. 8). We analysed the  
649 correlation of daily averaged observed IO during the three campaigns with daily averaged  
650 values of oceanic parameters (SST, chl-*a*, salinity, SSI concentration), meteorological  
651 parameters (wind speed, ozone) and calculated inorganic iodine fluxes. We divided the  
652 combined dataset from three campaigns into two regional subsets for the north (Fig. 8a) and  
653 south (Fig. 8b) of the polar front ( $47^\circ \text{S}$ ). The correlation for SSI concentrations is included for  
654 all the seven methods for SSI estimation listed in Sect. 2.3. The fluxes of HOI and  $\text{I}_2$  obtained  
655 using the seven different datasets for SSI are included and listed in Fig. 8 in the same order as  
656 the SSI concentration (labelled 1 to 7). IO model output from GEOS-Chem (labelled 8) and



657 CAM-Chem (labelled 9) is included for the correlation analysis, along with chl-*a* data from  
658 observations during ISOE-8 and ISOE-9 and satellite dataset obtained from MODIS Aqua  
659 (Oceancolor, NASA-GSFC, 2017).

660 For the entire dataset (Fig. 8c), only wind speed shows a statistically significant, positive  
661 correlation with observed IO above the 99 % confidence limit ( $R = 0.4$ ,  $P < 0.001$ ,  $n = 115$ ). A  
662 similar positive correlation with wind speed was found in the subset of data south of the polar  
663 front (Fig. 8b) ( $R = 0.49$ ,  $P = 0.01$ ,  $n = 48$ ), with observations north of the polar front showing  
664 a weaker positive correlation ( $R = 0.27$ ,  $P = 0.08$ ,  $n = 67$ ). Mahajan et al. (2012) showed that  
665 no correlation existed between IO and wind speed over the eastern Pacific Ocean, contrary to  
666 the results in this study. Current estimation methods for iodine emissions have a negative  
667 dependence on wind speed (Eq. 7 and 8). A positive correlation of IO with wind speed could  
668 suggest that increased vertical mixing enables emission of HOI and I<sub>2</sub>, and/or other iodine  
669 gases, thus enhancing IO production in the MBL. However, the interfacial model still over  
670 predicts IO concentrations at low wind speeds due to over prediction of HOI and I<sub>2</sub> emission  
671 (MacDonald et al., 2014). The apparently contradictory results from different studies call for  
672 more observations of IO in the MBL over a range of wind speeds.

673 Salinity and SST show a weak negative correlation with atmospheric IO for the entire dataset  
674 and for the north of the polar front region. This indicates that even if the physical parameters  
675 are significant for the initial parametrisation for SSI and inorganic flux estimation, there is no  
676 direct and significant correlation of these parameters with the atmospheric IO. However, south  
677 of the polar front, SST correlates positively above the 99 % limit ( $R = 0.52$ ,  $P = 0.01$ ,  $n = 48$ )  
678 and salinity correlates positively above the 95 % limit ( $R = 0.44$ ,  $P = 0.03$ ,  $n = 48$ ). Ozone  
679 correlates negatively with IO above 95 % limit ( $R = -0.4$ ,  $P = 0.046$ ,  $n = 47$ ), which could  
680 indicate catalytic destruction of tropospheric ozone through atmospheric iodine cycling in the



681 south of the polar front. This highlights that although these physical parameters may be  
682 required for iodine fluxes, IO levels may only be weakly related to them.

683 The calculated SSI concentrations and the HOI and I<sub>2</sub> fluxes calculated using these SSIs all  
684 show a significant negative correlation with the observed IO concentrations above the 95 %  
685 confidence limit for the entire dataset (except for the HOI flux estimated from the MacDonald  
686 et al. (2014) parameterisation, which shows no significant correlation). The positive correlation  
687 of the observed IO with wind speed is a potential driver for the negative correlation of observed  
688 IO with the calculated HOI and I<sub>2</sub> fluxes, which decrease with wind speed.

689 Measured iodide levels (labelled 4) and the I<sub>2</sub> and HOI fluxes calculated from them (also  
690 labelled 4) show no correlation with the observed IO levels across the entire dataset, although  
691 iodide shows a significant positive correlation ( $R = 0.55$ ,  $P = 0.04$ ,  $n = 32$ ) for IO measured  
692 south of the polar front. Mahajan et al. (2019a) pointed out that SST negatively correlated with  
693 IO for the ISOE-8 campaign, contradicting the previous results for observations in the Pacific  
694 Ocean (Großmann et al., 2013; Mahajan et al., 2012). Here, SST shows a significant positive  
695 correlation with observed IO ( $R = 0.52$ ,  $P = 0.006$ ,  $n = 48$ ) south of the polar front above the  
696 99 % confidence limit, but there is no correlation north of the polar front and only a weak  
697 negative correlation using the combined dataset from the three campaigns ( $R = -0.18$ ,  $P = 0.13$ ,  
698  $n = 119$ ).

699 Despite the above-mentioned point regarding the increase in observed IO levels in regions of  
700 elevated chl-*a*, there is only a weak and negative correlation of IO with chl-*a* (both from  
701 observations and satellite data) south of the polar front. However, there is a strong positive  
702 relationship north of the polar front ( $R = 0.696$ ,  $P = 2.3 \times 10^{-4}$ ,  $n = 29$ ). In fact, for the region  
703 north of the polar front, chl-*a* shows a significant positive correlation with observed IO above  
704 the 99 % confidence limit ( $P < 0.001$ ). The GEOS-Chem and CAM-Chem output also shows a



705 significant positive correlation (Fig. 8) which may result from the dependency of organic iodine  
706 species on oceanic chl-*a* in both GEOS-Chem and CAM-Chem. Figure 8 shows a large  
707 difference in correlation values for chl-*a* data obtained from observations and satellite (MODIS  
708 Aqua, NASA, GSFC; <https://oceancolor.gsfc.nasa.gov>). In situ, observed chl-*a* showed an  
709 improved correlation with IO compared to those with satellite chl-*a*. Figure 9 shows linear fits  
710 for chl-*a* from in situ observations and satellite against IO for the entire dataset and north of  
711 polar front subset. For the entire dataset, correlation of chl-*a* with IO from both observations  
712 and satellite data is not significant. Chl-*a* from in situ observations positively correlates with  
713 IO ( $R = 0.15$ ,  $P = 0.32$ ) while chl-*a* from satellite data correlates negatively ( $R = -0.13$ ,  $P =$   
714  $0.26$ ). Correlations of chl-*a* with IO improves for the north of polar front for chl-*a* from  
715 observations ( $R = 0.696$ ,  $P = 0.0002$ ), but chl-*a* from satellite data shows a statistically  
716 insignificant correlation with IO ( $R = 0.08$ ,  $P = 0.57$ ). The discrepancies in chl-*a* from  
717 observations and satellite data will make it difficult to identify links between the organic  
718 parameter and atmospheric IO and expand this to a global scale.

719 Despite the observed negative relationship of IO with wind speed noted above, note that the  
720 GEOS-Chem IO model output (which is dependent on the calculated HOI and I<sub>2</sub> fluxes) shows  
721 a significant positive correlation with observed IO above the 99 % confidence limit for data  
722 south ( $R = 0.78$ ,  $P = P < 0.001$ ,  $n = 48$ ) and north ( $R = 0.69$ ,  $P = P < 0.001$ ,  $n = 68$ ) of the polar  
723 front, although there is no correlation across the entire dataset. Note that the model  
724 underestimates IO values by 1 pptv south of the polar front and generally overestimates IO, by  
725 ~1.5 pptv, north of the polar front (Fig. 4). A linear fit for observed IO against modelled IO for  
726 north and south of the polar front (Fig. 10) shows significant positive correlation of GEOS-  
727 Chem output with observed IO, but with very different slopes north of the polar front (where  
728 the models overestimate IO) and south of the polar front (where the models underestimate IO).



729 Hence, even though the correlations are good in the individual regions, the model does not  
730 accurately reproduce the observed absolute concentrations.

## 731 **5. Conclusions**

732 In this study, region-specific parameterisation tools were devised for sea surface iodide (SSI)  
733 estimation following previous SSI estimation methods from Chance et al. (2014) and  
734 MacDonald et al. (2014). New observations of SSI from ISOE-9, SK-333 and BoBBLE (Indian  
735 and the Southern Ocean) were used to create region-specific SSI parameterisations. An average  
736 difference of up to 40 % in SSI concentration was observed among the existing  
737 parameterisations (Eq. 1, 4, and 6) and the difference was 21 % for the region-specific ones  
738 (Eq. 2, 3, and 5). Comparison of estimated SSI concentrations from various parameterisations  
739 with observed SSI and sensitivity to seasonal salinity changes showed that the modified Chance  
740 parameterisation (Eq. 2) was most suitable relative to the SST based parameterisation (Eq. 5)  
741 for SSI estimation in the Indian Ocean and Southern Ocean region. Since the existing global  
742 parameterisation schemes (Eq. 1 and 3) fail to match measured SSI in this region, it highlights  
743 the need to conduct more observations of SSI in the Indian Ocean and Southern Ocean region  
744 to fully understand and estimate the impact of seasonally varying, region-specific parameters  
745 (like salinity, reversing winds patterns) influencing the seawater iodide concentration in this  
746 region. Alternatively, a region-specific parameterisation scheme may be included in the global  
747 models for better representation of seawater iodine chemistry in the Indian and Southern Ocean  
748 region. Modelled estimates from Sherwen et al. (2019) also captured SSI well, although some  
749 high concentrations in the northern Indian Ocean region were not captured. SSI estimation from  
750 SST alone under-predicts SSI for the Indian Ocean, and so is not considered to be suitable for  
751 SSI estimation in the Indian Ocean region. Although, improving SSI concentration in models  
752 for the Indian Ocean and Southern Ocean region may improve the estimation of seawater iodine  
753 chemistry, it does not translate to estimating the atmospheric iodine chemistry in this region.



754 An accurate estimation of inorganic iodine fluxes (HOI and I<sub>2</sub>) is hence necessary to explain  
755 observed levels of IO in the remote open ocean marine boundary layer. However, these first  
756 concomitant observations of SSI and IO show that these inorganic fluxes, estimated in this  
757 study, fail to explain detected IO levels for the entire dataset. No significant correlation was  
758 seen between the SSI from different parameterisation techniques or estimated inorganic iodine  
759 fluxes with observed IO levels. Fluxes estimated using iodide from different parameterisation  
760 and measured iodide did not show large variation in values and followed a similar latitudinal  
761 trend. This is indicative that the inorganic iodine flux parameterisation is not highly sensitive  
762 to the SSI parameterisation. Predicted inorganic iodine fluxes did not explain iodine chemistry,  
763 as indicated by IO levels, in the atmosphere above the Indian and Southern Ocean (Indian  
764 Ocean sector). Chl-*a* shows a positive correlation with IO for the north of the polar front region,  
765 suggesting that biologically emitted species could also play a role in addition to ozone and  
766 iodide derived inorganic emissions of HOI and I<sub>2</sub>. Finally, model predictions of IO  
767 underestimate IO levels for the Southern Ocean region but overestimate IO in the Indian Ocean.  
768 Models greatly underestimate IO in regions with higher chl-*a* concentration which could be  
769 indicative of organic species playing a role (close to the Kerguelen Islands, refer Sect. 3.4.2).  
770 This study suggests that the fluxes of iodine in the MBL are more complex than considered at  
771 present and further studies are necessary in order to parameterise accurate inorganic and  
772 organic fluxes that can be used in models. Using seawater iodide measurements and  
773 calculations from different parameterisations did not alter the inorganic iodide flux estimate  
774 greatly. Direct observations of HOI and I<sub>2</sub>, alongside volatile organic iodine measurements in  
775 the MBL are necessary in order to reduce the uncertainty in the impacts of iodine chemistry.

776 **6. Author contributions:**

777 ASM conceptualised the research plan and methodology. SI did the data curation, analysis, and  
778 writing of the original draft. LT and RC did the iodide measurements provided unpublished





779 iodide data from ISOE-9, SK-333 and BoBBLE. PS and RCo provided salinity data for ISOE-  
780 9. SCT and AUK provided chl-a data for ISOE-9. AKS and PVB provided chl-a data for SK-  
781 333. AS and RR provided chl-a data from BoBBLE. CC and ASL did the CAM-Chem model  
782 run for ISOE-9 and IIOE-2. TS did the GEOS-Chem model run for ISOE-9, IIOE-2 and ISOE-  
783 8.

## 784 **7. Acknowledgements**

785 The authors thank the Ministry of Earth Sciences for funding the expeditions and IITM for  
786 providing research fellowship to Swaleha Inamdar. We would particularly like to thank the  
787 ISOE and IIOE-2 teams for their tireless contribution in manually recording and compiling  
788 atmospheric and oceanic observations during the expedition. We express gratitude towards the  
789 officers, crew and scientist on board RV S. A. Agulhas and RV Sagar Kanya ships for their  
790 support. LJC, LT, RC and TS thank the UK NERC (NE/N009983/1) for funding.

## 791 **8. References**

- 792 Alicke, B., Hebestreit, K., Stutz, J. and Platt, U.: Iodine oxide in the marine boundary layer,  
793 *Nature*, 397, 572–3, doi:10.1038/17508, 1999.
- 794 Allan, B. J., McFiggans, G., Plane, J. M. C. and Coe, H.: Observations of iodine monoxide in  
795 the remote marine boundary layer, *J. Geophys. Res. Atmos.*, doi:10.1029/1999JD901188,  
796 2000.
- 797 Atkinson, H. M., Huang, R.-J., Chance, R., Roscoe, H. K., Hughes, C., Davison, B.,  
798 Schönhardt, A., Mahajan, A. S., Saiz-Lopez, A., Hoffmann, T. and Liss, P. S.: Iodine  
799 emissions from the sea ice of the Weddell Sea, *Atmos. Chem. Phys.*, 12(22), 11229–11244,  
800 doi:10.5194/acp-12-11229-2012, 2012.
- 801 Bogumil, K., Orphal, J., Homann, T., Voigt, S., Spietz, P., Fleischmann, O. C., Vogel, A.,



- 802 Hartmann, M., Kromminga, H., Bovensmann, H., Frerick, J. and Burrows, J. P.:
- 803 Measurements of molecular absorption spectra with the SCIAMACHY pre-flight model:
- 804 Instrument characterization and reference data for atmospheric remote-sensing in the 230-
- 805 2380 nm region, *J. Photochem. Photobiol. A Chem.*, 157(2–3), 167–184, doi:10.1016/S1010-
- 806 6030(03)00062-5, 2003.
- 807 Campos, M. L. A. M.: New approach to evaluating dissolved iodine speciation in natural
- 808 waters using cathodic stripping voltammetry and a storage study for preserving iodine
- 809 species, *Mar. Chem.*, 57(1–2), 107–117, doi:10.1016/S0304-4203(96)00093-X, 1997.
- 810 Carpenter, L. J.: Iodine in the Marine Boundary Layer, *Chem. Rev.*, 103(12), 4953–4962,
- 811 doi:10.1021/cr0206465, 2003.
- 812 Carpenter, L. J., MacDonald, S. M., Shaw, M. D., Kumar, R., Saunders, R. W., Parthipan, R.,
- 813 Wilson, J. and Plane, J. M. C.: Atmospheric iodine levels influenced by sea surface emissions
- 814 of inorganic iodine, *Nat. Geosci.*, 6(2), 108–111, doi:10.1038/ngeo1687, 2013.
- 815 Chameides, W. L. and Davis, D. D.: Iodine : Its Possible Role in Tropospheric
- 816 Photochemistry, *J. Geophys. Res. Ocean.*, 85(C12), 7383–7398,
- 817 doi:10.1029/JC085iC12p07383, 1980.
- 818 Chance, K. V. and Spurr, R. J. D.: Ring effect studies: Rayleigh scattering, including
- 819 molecular parameters for rotational Raman scattering, and the Fraunhofer spectrum, *Appl.*
- 820 *Opt.*, 36(21), 5224–5230, doi:10.1364/AO.36.005224, 1997.
- 821 Chance, R., Baker, A. R., Carpenter, L. and Jickells, T. D.: The distribution of iodide at the
- 822 sea surface, *Environ. Sci. Process. Impacts*, 16(8), 1841–1859, doi:10.1039/C4EM00139G,
- 823 2014.
- 824 Chance, R., Tinel, L., Sherwen, T., Baker, A., Bell, T., Brindle, J., Campos, M. L. A. M.,



- 825 Croot, P., Ducklow, H., He, P., Hoogakker, B., Hopkins, F. E., Hughes, C., Jickells, T.,  
826 Loades, D., Macaya, D. A., Mahajan, A. S., Malin, G., Phillips, D. P., Sinha, A. K., Sarkar,  
827 A., Roberts, I. J., Roy, R., Song, X., Winklebauer, H. A., Wuttig, K., Yang, M., Zhou, P. and  
828 Carpenter, L. J.: Global sea-surface iodide observations, 1967-2018, submitted,  
829 doi:10.5285/7e77d6b9-83fb-41e0-e053-6c86abc069d0, 2019a.
- 830 Chance, R., Tinel, L., Carpenter, L. J., Sarkar, A., Sinha, A. K., Mahajan, A. S., Chacko, R.,  
831 Sabu, P., Roy, R., Jickells, T. D., Stevens, D. and Wadley, M.: Surface inorganic iodine  
832 speciation in the Indian Ocean and Indian Ocean sector of the Southern Ocean, Manuscr.  
833 Prep., 2019b.
- 834 Chang, W., Heikes, B. G. and Lee, M.: Ozone deposition to the sea surface: chemical  
835 enhancement and wind speed dependence, *Atmos. Environ.*, 38(7), 1053–1059,  
836 doi:10.1016/j.atmosenv.2003.10.050, 2004.
- 837 D’Addezio, J. M., Subrahmanyam, B., Nyadjro, E. S. and Murty, V. S. N.: Seasonal  
838 Variability of Salinity and Salt Transport in the Northern Indian Ocean, *J. Phys. Oceanogr.*,  
839 45(7), 1947–1966, doi:10.1175/JPO-D-14-0210.1, 2015.
- 840 Danckaert, T., Fayt, C. and Van Roozendaal, M.: QDOAS 3.2. [online] Available from:  
841 [http://uv-vis.aeronomie.be/software/QDOAS/QDOAS\\_manual.pdf](http://uv-vis.aeronomie.be/software/QDOAS/QDOAS_manual.pdf), 2017.
- 842 Davis, D., Crawford, J., Liu, S., McKeen, S., Bandy, A., Thornton, D., Rowland, F. and  
843 Blake, D.: Potential impact of iodine on tropospheric levels of ozone and other critical  
844 oxidants, *J. Geophys. Res. Atmos.*, 101(D1), 2135–2147, doi:10.1029/95JD02727, 1996.
- 845 Dinesh Kumar, P. K., Paul, Y. S., Muraleedharan, K. R., Murty, V. S. N. and Preenu, P. N.:  
846 Comparison of long-term variability of Sea Surface Temperature in the Arabian Sea and Bay  
847 of Bengal, *Reg. Stud. Mar. Sci.*, 3, 67–75, doi:10.1016/j.rsma.2015.05.004, 2016.



- 848 Farrenkopf, A. M. and Luther, G. W.: Iodine chemistry reflects productivity and  
849 denitrification in the Arabian Sea: evidence for flux of dissolved species from sediments of  
850 western India into the OMZ, *Deep Sea Res. Part II Top. Stud. Oceanogr.*, 49(12), 2303–2318,  
851 doi:10.1016/S0967-0645(02)00038-3, 2002.
- 852 Frieß, U., Wagner, T., Pundt, I., Pfeilsticker, K. and Platt, U.: Spectroscopic measurements of  
853 tropospheric iodine oxide at Neumayer station, Antarctica, *Geophys. Res. Lett.*, 28(10),  
854 1941–1944, doi:10.1029/2000GL012784, 2001.
- 855 Gálvez, Ó., Teresa Baeza-Romero, M., Sanz, M. and Pacios, L. F.: A theoretical study on the  
856 reaction of ozone with aqueous iodide, *Phys. Chem. Chem. Phys.*, 18(11), 7651–7660,  
857 doi:10.1039/c5cp06440f, 2016.
- 858 Ganzeveld, L., Helmig, D., Fairall, C. W., Hare, J. and Pozzer, A.: Atmosphere-ocean ozone  
859 exchange: A global modeling study of biogeochemical, atmospheric, and waterside  
860 turbulence dependencies, *Global Biogeochem. Cycles*, 23(4), 1–16,  
861 doi:10.1029/2008GB003301, 2009.
- 862 Garland, J. A., Elzerman, A. W. and Penkett, S. A.: The mechanism for dry deposition of  
863 ozone to seawater surfaces, *J. Geophys. Res. Ocean.*, 85(C12), 7488–7492,  
864 doi:10.1029/JC085iC12p07488, 1980.
- 865 Großmann, K., Frieß, U., Peters, E., Wittrock, F., Lampel, J., Yilmaz, S., Tschirner, J.,  
866 Sommariva, R., von Glasow, R., Quack, B., Krüger, K., Pfeilsticker, K. and Platt, U.: Iodine  
867 monoxide in the Western Pacific marine boundary layer, *Atmos. Chem. Phys.*, 13(6), 3363–  
868 3378, doi:10.5194/acp-13-3363-2013, 2013.
- 869 Hönninger, G., von Friedeburg, C. and Platt, U.: Multi Axis Differential Optical Absorption  
870 Spectroscopy (MAX-DOAS), *Atmos. Chem. Phys. Discuss.*, 3(6), 5595–5658,  
871 doi:10.5194/acpd-3-5595-2003, 2004.



- 872 Hossaini, R., Chipperfield, M. P., Saiz-Lopez, A., Fernandez, R., Monks, S., Feng, W.,  
873 Brauer, P. and Von Glasow, R.: A global model of tropospheric chlorine chemistry: Organic  
874 versus inorganic sources and impact on methane oxidation, *J. Geophys. Res.*, 121(23),  
875 14,271–14,297, doi:10.1002/2016JD025756, 2016.
- 876 Huang, R. J., Seitz, K., Neary, T., O’Dowd, C. D., Platt, U. and Hoffmann, T.: Observations  
877 of high concentrations of I<sub>2</sub> and IO in coastal air supporting iodine-oxide driven coastal new  
878 particle formation, *Geophys. Res. Lett.*, 37(3), 1–5, doi:10.1029/2009GL041467, 2010.
- 879 Jenkin, M. E., Cox, R. A., Candeland, D. E. and Division, M. S.: Photochemical aspects of  
880 tropospheric iodine behaviour, *J. Atmos. Chem.*, 2(4), 359–375, doi:10.1007/BF00130748,  
881 1985.
- 882 Koenig, T. K., Baidar, S., Campuzano-Jost, P., Cuevas, C. A., Dix, B., Fernandez, R. P., Guo,  
883 H., Hall, S. R., Kinnison, D., Nault, B. A., Ullmann, K., Jimenez, J. L., Saiz-Lopez, A. and  
884 Volkamer, R.: Quantitative detection of iodine in the stratosphere, *Proc. Natl. Acad. Sci.*,  
885 (15), 201916828, doi:10.1073/pnas.1916828117, 2020.
- 886 Lawler, M. J., Mahajan, A. S., Saiz-Lopez, A. and Saltzman, E. S.: Observations of I<sub>2</sub> at a  
887 remote marine site, *Atmos. Chem. Phys.*, 14, 2669–2678, doi:10.5194/acp-14-2669-2014,  
888 2014a.
- 889 Lawler, M. J., Mahajan, A. S., Saiz-Lopez, A. and Saltzman, E. S.: Observations of I<sub>2</sub> at a  
890 remote marine site, *Atmos. Chem. Phys.*, doi:10.5194/acp-14-2669-2014, 2014b.
- 891 Luther, G. W., Swartz, C. B. and Ullman, W. J.: Direct determination of iodide in seawater  
892 by cathodic stripping square wave voltammetry, *Anal. Chem.*, 60(17), 1721–1724,  
893 doi:10.1021/ac00168a017, 1988.
- 894 MacDonald, S. M., Gómez Martín, J. C., Chance, R., Warriner, S., Saiz-Lopez, A.,



- 895 Carpenter, L. J. and Plane, J. M. C.: A laboratory characterisation of inorganic iodine  
896 emissions from the sea surface: Dependence on oceanic variables and parameterisation for  
897 global modelling, *Atmos. Chem. Phys.*, 14(11), 5841–5852, doi:10.5194/acp-14-5841-2014,  
898 2014.
- 899 Mahajan, A. S., Oetjen, H., Saiz-Lopez, A., Lee, J. D., McFiggans, G. B. and Plane, J. M. C.:  
900 Reactive iodine species in a semi-polluted environment, *Geophys. Res. Lett.*, 36(16), L16803,  
901 doi:10.1029/2009GL038018, 2009.
- 902 Mahajan, A. S., Shaw, M., Oetjen, H., Hornsby, K. E., Carpenter, L. J., Kaleschke, L., Tian-  
903 Kunze, X., Lee, J. D., Moller, S. J., Edwards, P., Commane, R., Ingham, T., Heard, D. E. and  
904 Plane, J. M. C.: Evidence of reactive iodine chemistry in the Arctic boundary layer, *J.*  
905 *Geophys. Res.*, 115(D20), D20303, doi:10.1029/2009JD013665, 2010a.
- 906 Mahajan, A. S., Plane, J. M. C., Oetjen, H., Mendes, L., Saunders, R. W., Saiz-Lopez, A.,  
907 Jones, C. E., Carpenter, L. J. and McFiggans, G. B.: Measurement and modelling of  
908 tropospheric reactive halogen species over the tropical Atlantic Ocean, *Atmos. Chem. Phys.*,  
909 10(10), 4611–4624, doi:10.5194/acp-10-4611-2010, 2010b.
- 910 Mahajan, A. S., Gómez Martín, J. C., Hay, T. D., Royer, S.-J., Yvon-Lewis, S., Liu, Y., Hu,  
911 L., Prados-Roman, C., Ordóñez, C., Plane, J. M. C. and Saiz-Lopez, A.: Latitudinal  
912 distribution of reactive iodine in the Eastern Pacific and its link to open ocean sources,  
913 *Atmos. Chem. Phys.*, 12(23), 11609–11617, doi:10.5194/acp-12-11609-2012, 2012.
- 914 Mahajan, A. S., Tinel, L., Hulswar, S., Cuevas, C. A., Wang, S., Ghude, S., Naik, R. K.,  
915 Mishra, R. K., Sabu, P., Sarkar, A., Anilkumar, N. and Saiz Lopez, A.: Observations of  
916 iodine oxide in the Indian Ocean Marine Boundary Layer: a transect from the tropics to the  
917 high latitudes, *Atmos. Environ. X*, 1(January), 100016, doi:10.1016/j.aeaoa.2019.100016,  
918 2019a.



- 919 Mahajan, A. S., Tinel, L., Sarkar, A., Chance, R., Carpenter, L. J., Hulswar, S., Mali, P.,  
920 Prakash, S. and Vinayachandran, P. N.: Understanding Iodine Chemistry Over the Northern  
921 and Equatorial Indian Ocean, *J. Geophys. Res. Atmos.*, (x), 2018JD029063,  
922 doi:10.1029/2018JD029063, 2019b.
- 923 McFiggans, G.: Marine aerosols and iodine emissions, *Nature*, 433(7026), E13–E13,  
924 doi:10.1038/nature03372, 2005.
- 925 Monterey, G. and Levitus, S.: Seasonal Variability of Mixed Layer Depth for the World  
926 Ocean. [online] Available from: <http://www.nodc.noaa.gov>, 1997.
- 927 O’Dowd, C. D., Jimenez, J. L., Bahreini, R., Flagan, R. C., Seinfeld, J. H., Hämeri, K.,  
928 Pirjola, L., Kulmala, M., Jennings, S. G. and Hoffmann, T.: Marine aerosol formation from  
929 biogenic iodine emissions, *Nature*, 417(6889), 632–636, doi:10.1038/nature00775, 2002.
- 930 Ordóñez, C., Lamarque, J.-F., Tilmes, S., Kinnison, D. E., Atlas, E. L., Blake, D. R., Sousa  
931 Santos, G., Brasseur, G. and Saiz-Lopez, A.: Bromine and iodine chemistry in a global  
932 chemistry-climate model: description and evaluation of very short-lived oceanic sources,  
933 *Atmos. Chem. Phys.*, 12(3), 1423–1447, doi:10.5194/acp-12-1423-2012, 2012.
- 934 Platt, U. and Stutz, J.: Differential Absorption Spectroscopy, in *Differential Optical*  
935 *Absorption Spectroscopy*, pp. 135–174, Springer, Berlin, Heidelberg., 2008.
- 936 Pope, R. M. and Fry, E. S.: Absorption spectrum (380–700 nm) of pure water. II. Integrating  
937 cavity measurements, *Appl. Opt.*, 36(33), 8710, doi:10.1364/AO.36.008710, 1997.
- 938 Prados-Roman, C., Cuevas, C. A., Hay, T., Fernandez, R. P., Mahajan, A. S., Royer, S. J.,  
939 Galí, M., Simó, R., Dachs, J., Großmann, K., Kinnison, D. E., Lamarque, J. F. and Saiz-  
940 Lopez, A.: Iodine oxide in the global marine boundary layer, *Atmos. Chem. Phys.*, 15(2),  
941 583–593, doi:10.5194/acp-15-583-2015, 2015.



- 942 Rao, R. R. and Sivakumar, R.: Seasonal variability of sea surface salinity and salt budget of  
943 the mixed layer of the north Indian Ocean, *J. Geophys. Res.*, 108(C1), 3009,  
944 doi:10.1029/2001JC000907, 2003.
- 945 Read, K. A., Mahajan, A. S., Carpenter, L. J., Evans, M. J., Faria, B. V. E., Heard, D. E.,  
946 Hopkins, J. R., Lee, J. D., Moller, S. J., Lewis, A. C., Mendes, L. M., McQuaid, J. B., Oetjen,  
947 H., Saiz-Lopez, A., Pilling, M. J. and Plane, J. M. C.: Extensive halogen-mediated ozone  
948 destruction over the tropical Atlantic Ocean, *Nature*, 453(7199), 1232–1235, 2008.
- 949 Rolph, G., Stein, A. and Stunder, B.: Real-time Environmental Applications and Display  
950 sYstem: READY, *Environ. Model. Softw.*, 95, 210–228, doi:10.1016/j.envsoft.2017.06.025,  
951 2017.
- 952 Rothman, L. S., Gordon, I. E., Babikov, Y., Barbe, A., Chris Benner, D., Bernath, P. F., Birk,  
953 M., Bizzocchi, L., Boudon, V., Brown, L. R., Campargue, A., Chance, K., Cohen, E. A.,  
954 Coudert, L. H., Devi, V. M., Drouin, B. J., Fayt, A., Flaud, J. M., Gamache, R. R., Harrison,  
955 J. J., Hartmann, J. M., Hill, C., Hodges, J. T., Jacquemart, D., Jolly, A., Lamouroux, J., Le  
956 Roy, R. J., Li, G., Long, D. A., Lyulin, O. M., Mackie, C. J., Massie, S. T., Mikhailenko, S.,  
957 Müller, H. S. P., Naumenko, O. V., Nikitin, A. V., Orphal, J., Perevalov, V., Perrin, A.,  
958 Polovtseva, E. R., Richard, C., Smith, M. A. H., Starikova, E., Sung, K., Tashkun, S.,  
959 Tennyson, J., Toon, G. C., Tyuterev, V. G. and Wagner, G.: The HITRAN2012 molecular  
960 spectroscopic database, *J. Quant. Spectrosc. Radiat. Transf.*, 130, 4–50,  
961 doi:10.1016/j.jqsrt.2013.07.002, 2013.
- 962 Saiz-Lopez, a, Shillito, J. a, Coe, H. and Plane, J. M. C.: Measurements and modelling of I<sub>2</sub>,  
963 IO, OIO, BrO and NO<sub>3</sub> in the mid-latitude marine boundary layer, *Atmos. Chem. Phys.*, 6(6),  
964 1513–1528, doi:10.5194/acp-6-1513-2006, 2006a.
- 965 Saiz-Lopez, A. and Plane, J. M. C.: Novel iodine chemistry in the marine boundary layer,





- 966 Geophys. Res. Lett., 31(4), L04112, doi:10.1029/2003GL019215, 2004.
- 967 Saiz-Lopez, A., Plane, J. M. C., McFiggans, G. B., Williams, P. I., Ball, S. M., Bitter, M.,  
968 Jones, R. L., Hongwei, C. and Hoffmann, T.: Modelling molecular iodine emissions in a  
969 coastal marine environment: the link to new particle formation, Atmos. Chem. Phys.  
970 Discuss., 5(4), 5405–5439, doi:10.5194/acpd-5-5405-2005, 2006b.
- 971 Saiz-Lopez, A., Plane, J. M. C., Baker, A. R., Carpenter, L. J., von Glasow, R., Gómez  
972 Martín, J. C., McFiggans, G. and Saunders, R. W.: Atmospheric Chemistry of Iodine, Chem.  
973 Rev., 112(3), 1773–1804, doi:10.1021/cr200029u, 2012.
- 974 Saiz-Lopez, A., Fernandez, R. P., Ordóñez, C., Kinnison, D. E., Martín, J. C. G., Lamarque,  
975 J. F. and Tilmes, S.: Iodine chemistry in the troposphere and its effect on ozone, Atmos.  
976 Chem. Phys., 14(23), 13119–13143, doi:10.5194/acp-14-13119-2014, 2014.
- 977 Saiz-Lopez, A. and Fernandez, R. P.: On the formation of tropical rings of atomic halogens:  
978 Causes and implications, Geophys. Res. Lett., 43(6), 2928–2935,  
979 doi:10.1002/2015GL067608, 2016.
- 980 Shenoi, S. S. C.: Differences in heat budgets of the near-surface Arabian Sea and Bay of  
981 Bengal: Implications for the summer monsoon, J. Geophys. Res., 107(C6), 3052,  
982 doi:10.1029/2000JC000679, 2002.
- 983 Sherwen, T., Schmidt, J. A., Evans, M. J., Carpenter, L. J., Großmann, K., Eastham, S. D.,  
984 Jacob, D. J., Dix, B., Koenig, T. K., Sinreich, R., Ortega, I., Volkamer, R., Saiz-Lopez, A.,  
985 Prados-Roman, C., Mahajan, A. S. and Ordóñez, C.: Global impacts of tropospheric halogens  
986 (Cl, Br, I) on oxidants and composition in GEOS-Chem, Atmos. Chem. Phys., 16(18),  
987 12239–12271, doi:10.5194/acp-16-12239-2016, 2016a.
- 988 Sherwen, T., Evans, M. J., Spracklen, D. V., Carpenter, L. J., Chance, R., Baker, A. R.,



- 989 Schmidt, J. A. and Breider, T. J.: Global modeling of tropospheric iodine aerosol, *Geophys.*  
990 *Res. Lett.*, 43(18), 10012–10019, doi:10.1002/2016GL070062, 2016b.
- 991 Sherwen, T., Evans, M. J., Carpenter, L. J., Andrews, S. J., Lidster, R. T., Dix, B., Koenig, T.  
992 K., Sinreich, R., Ortega, I., Volkamer, R., Saiz-Lopez, A., Prados-Roman, C., Mahajan, A. S.  
993 and Ordóñez, C.: Iodine’s impact on tropospheric oxidants: a global model study in GEOS-  
994 *Chem, Atmos. Chem. Phys.*, 16(2), 1161–1186, doi:10.5194/acp-16-1161-2016, 2016c.
- 995 Sherwen, T., Evans, M. J., Sommariva, R., Hollis, L. D. J., Ball, S. M., Monks, P. S., Reed,  
996 C., Carpenter, L. J., Lee, J. D., Forster, G., Bandy, B., Reeves, C. E. and Bloss, W. J.: Effects  
997 of halogens on European air-quality, *Faraday Discuss.*, 200(February), 75–100,  
998 doi:10.1039/C7FD00026J, 2017.
- 999 Sherwen, T., Chance, R. J., Tinel, L., Ellis, D., Evans, M. J. and Carpenter, L. J.: A machine-  
1000 learning-based global sea-surface iodide distribution, *Earth Syst. Sci. Data*, 11(3), 1239–  
1001 1262, doi:10.5194/essd-11-1239-2019, 2019a.
- 1002 Sherwen, T., Chance, R. J., Tinel, L., Ellis, D., Evans, M. J. and Carpenter, L. J.: A machine  
1003 learning based global sea-surface iodide distribution, *Earth Syst. Sci. Data Discuss.*, 1–40,  
1004 doi:10.5194/essd-2019-40, 2019b.
- 1005 Simpson, W. R., Brown, S. S., Saiz-Lopez, A., Thornton, J. A. and Von Glasow, R.:  
1006 Tropospheric Halogen Chemistry: Sources, Cycling, and Impacts, *Chem. Rev.*, 115(10),  
1007 4035–4062, doi:10.1021/cr5006638, 2015.
- 1008 Sinreich, R., Coburn, S., Dix, B. and Volkamer, R.: Ship-based detection of glyoxal over the  
1009 remote tropical Pacific Ocean, *Atmos. Chem. Phys.*, 10(23), 11359–11371, doi:10.5194/acp-  
1010 10-11359-2010, 2010.
- 1011 Stein, A. F., Draxler, R. R., Rolph, G. D., Stunder, B. J. B., Cohen, M. D. and Ngan, F.:



- 1012 Noaa's hysplit atmospheric transport and dispersion modeling system, *Bull. Am. Meteorol.*  
1013 *Soc.*, 96(12), 2059–2077, doi:10.1175/BAMS-D-14-00110.1, 2015.
- 1014 Stone, D., Sherwen, T., Evans, M. J., Vaughan, S., Ingham, T., Whalley, L. K., Edwards, P.  
1015 M., Read, K. A., Lee, J. D., Moller, S. J., Carpenter, L. J., Lewis, A. C. and Heard, D. E.:  
1016 Impacts of bromine and iodine chemistry on tropospheric OH and HO<sub>2</sub>: Comparing  
1017 observations with box and global model perspectives, *Atmos. Chem. Phys.*, doi:10.5194/acp-  
1018 18-3541-2018, 2018.
- 1019 Thalman, R. and Volkamer, R. A.: Temperature dependent absorption cross-sections of O<sub>2</sub>-O  
1020 2 collision pairs between 340 and 630 nm and at atmospherically relevant pressure, *Phys.*  
1021 *Chem. Chem. Phys.*, 15(37), 15371–15381, doi:10.1039/c3cp50968k, 2013.
- 1022 Vandaele, A. C., Hermans, C., Simon, P. C., Carleer, M., Colin, R., Fally, S., Mérienne, M.  
1023 F., Jenouvrier, A. and Coquart, B.: Measurements of the NO<sub>2</sub> absorption cross-section from  
1024 42000 cm<sup>-1</sup> to 10000 cm<sup>-1</sup> (238–1000 nm) at 220 K and 294 K, *J. Quant. Spectrosc. Radiat.*  
1025 *Transf.*, 59(3–5), 171–184, doi:10.1016/S0022-4073(97)00168-4, 1998.
- 1026 Vogt, R., Sander, R., Von Glasow, R. and Crutzen, P. J.: Iodine chemistry and its role in  
1027 halogen activation and ozone loss in the marine boundary layer: A model study, *J. Atmos.*  
1028 *Chem.*, 32(3), 375–395, doi:10.1023/A:1006179901037, 1999.
- 1029 Wagner, T., Dix, B., Friedeburg, C. V., Frieß, U., Sanghavi, S., Sinreich, R. and Platt, U.:  
1030 MAX-DOAS O<sub>4</sub> measurements: A new technique to derive information on atmospheric  
1031 aerosols - Principles and information content, *J. Geophys. Res. D Atmos.*, 109(22), 1–19,  
1032 doi:10.1029/2004JD004904, 2004.
- 1033 Wagner, T., Beirle, S. and Deutschmann, T.: Three-dimensional simulation of the Ring effect  
1034 in observations of scattered sun light using Monte Carlo radiative transfer models. [online]  
1035 Available from: [www.atmos-meas-tech.net/2/113/2009/](http://www.atmos-meas-tech.net/2/113/2009/) (Accessed 16 January 2019), 2009.

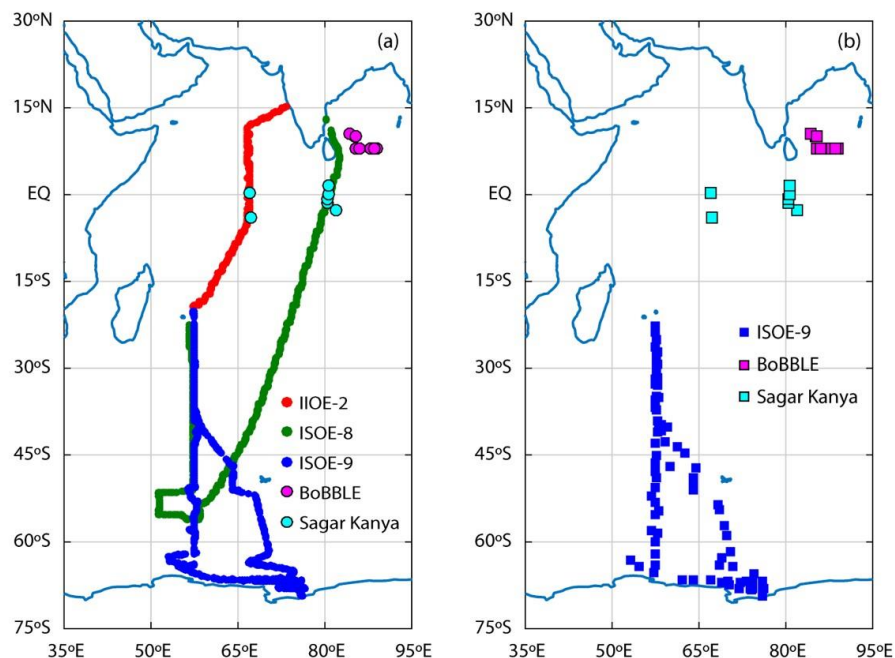


1036

1037

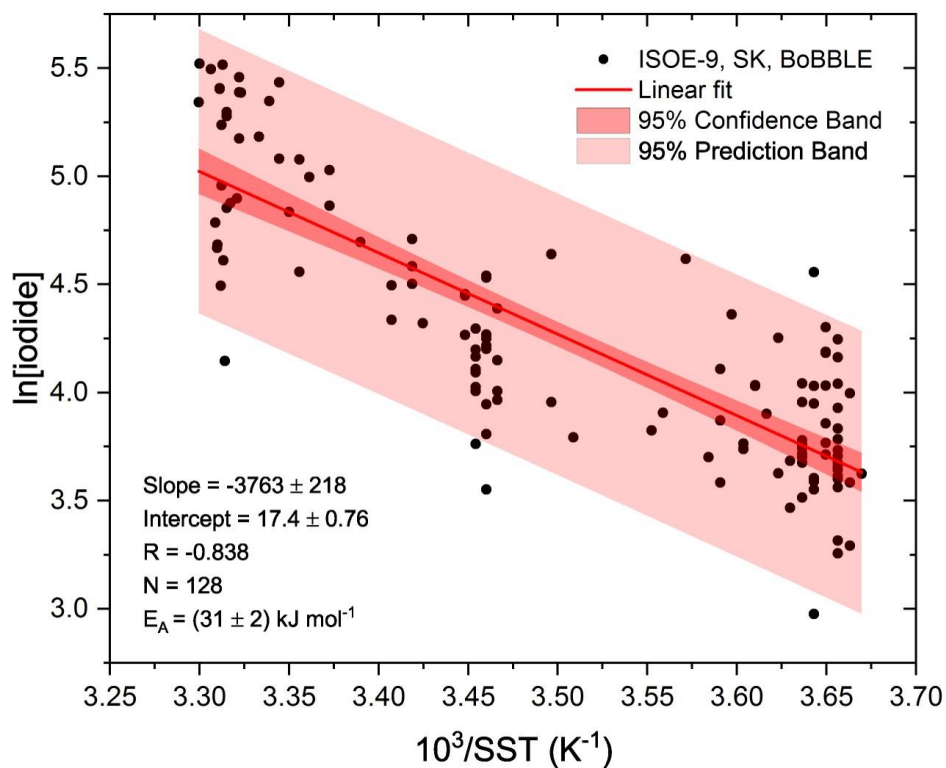


1038 9. Figures



1039

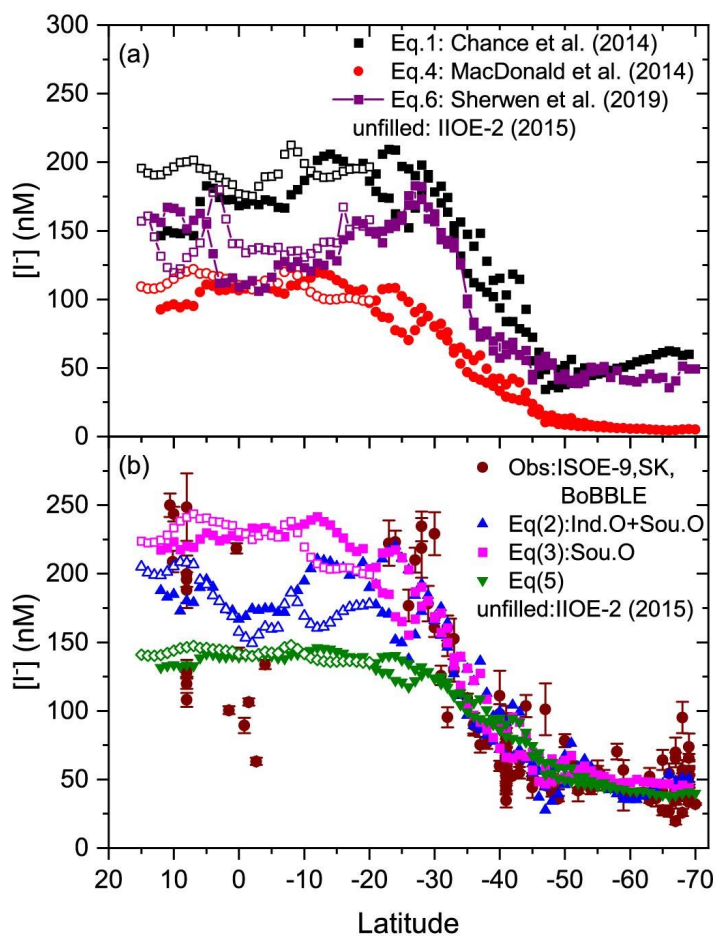
1040 **Figure 1:** Map of the Indian Ocean and the Southern Ocean (a) with cruise tracks for  
1041 campaigns conducted during the austral summer of 2014-2016. Green circles indicate the  
1042 cruise track for ISOE-8, red circles show the cruise track for IIOE-2, and blue circles  
1043 indicate the cruise track for ISOE-9. Magenta and cyan circles indicate sample locations  
1044 for the BoBBLE and SK-333 expeditions respectively. (b) boxes represent 129 seawater  
1045 iodide sampling locations from 3 expeditions following the colour code in (a).



1046

1047 **Figure 2: Arrhenius form plot of sea surface iodide concentrations against SST from all**  
1048 **available seawater iodide field observations in the Indian Ocean and Southern Ocean.**  
1049 **The red line represents a linear fit., the shaded region in dark red (inner) indicates the**  
1050 **95% confidence bands and shaded area in light red (outer) indicates the 95% prediction**  
1051 **bands.**

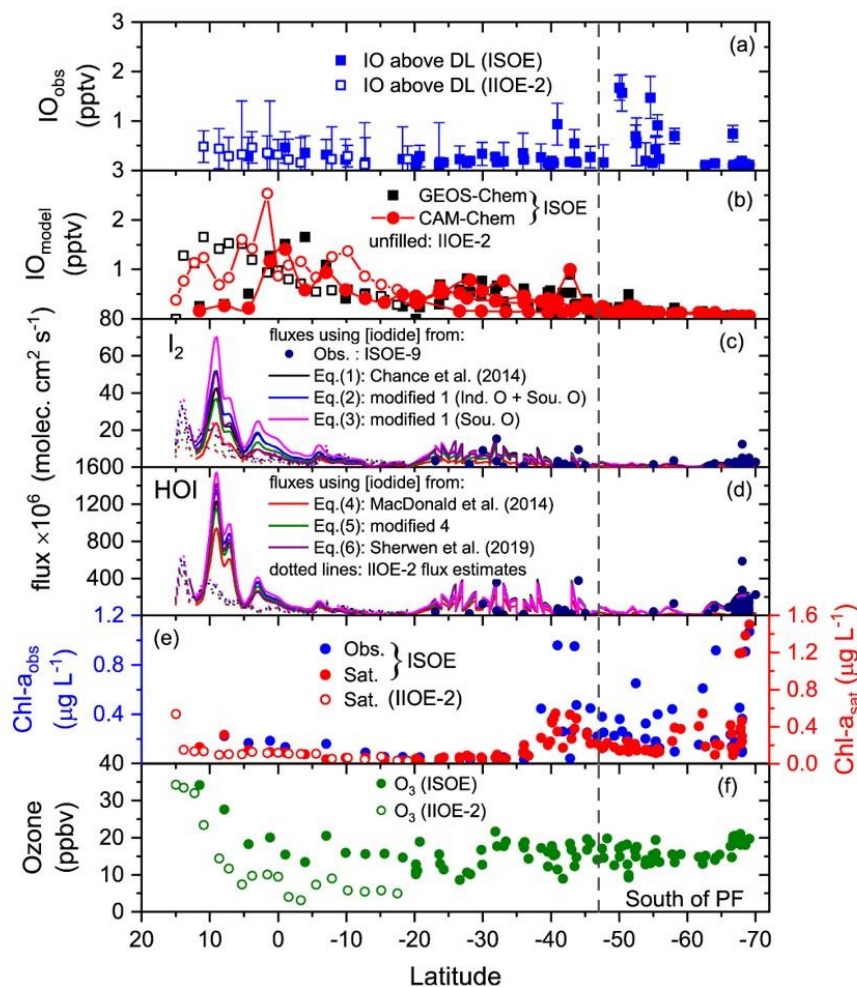
1052



1053

1054 **Figure 3: Latitudinal averages of calculated sea surface iodide (SSI) concentrations for**  
1055 **each campaign using (a) existing, (b) new parameterisation tools and observations from**  
1056 **ISOE-9, SK-333, and BoBBLE. Filled markers represent combined SSI from ISOE-8 and**  
1057 **ISOE-9, unfilled markers represent SSI from IIOE-2 campaign.**

1058



1059

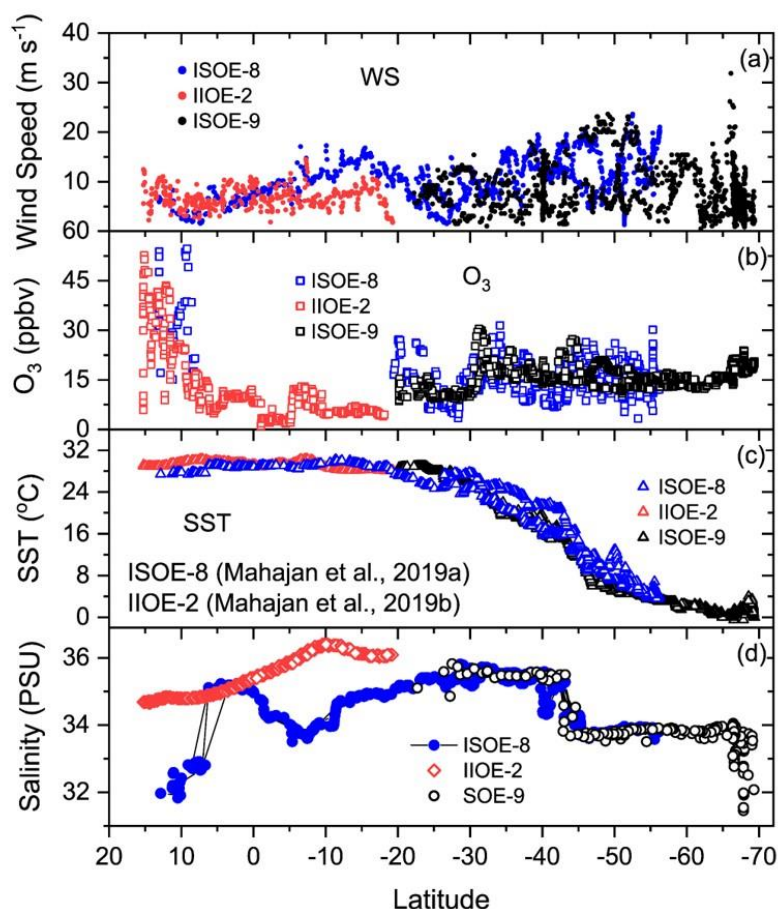
1060 **Figure 4: Daily averaged atmospheric and oceanic parameters combined from ISOE-8,**  
 1061 **IIOE-2, and ISOE-9 field campaigns. Data marked ISOE represents combined data from**  
 1062 **ISOE-8 and ISOE-9. Unfilled markers and dotted lines show values for IIOE-2. (a) IO**  
 1063 **above detection limit from ISOE-8, ISOE-9 and IIOE-2. (b) Surface IO values from**  
 1064 **GEOS-Chem and CAM-Chem models. (c) and (d) comprise of HOI and  $I_2$  fluxes**  
 1065 **estimated from Eq. (7) and (6) respectively. Fluxes are colour coded for different sea**  
 1066 **surface iodide (SSI) datasets used for their estimation. Colours black, blue, red and green**  
 1067 **correspond to fluxes calculated using SSI estimation from Eq. (1) to (5), purple colour**  
 1068 **represents the use of model SSI predictions (Sherwen et al., 2019b), filled circles in dark**  
 1069 **blue correspond to measured SSI from ISOE-9 for each observation, (e) chlorophyll-*a***  
 1070 **observations from ISOE-8 and ISOE-9 (blue circles) and satellite data for all campaigns**  
 1071 **(red circles). (f) ozone mixing ratios from campaigns ISOE and IIOE-2. The dashed line**





1072 marks the polar front at 47° S. Observational plots for ISOE-8 and IIOE-2 were adapted  
1073 from Mahajan et al. 2019 a & b.

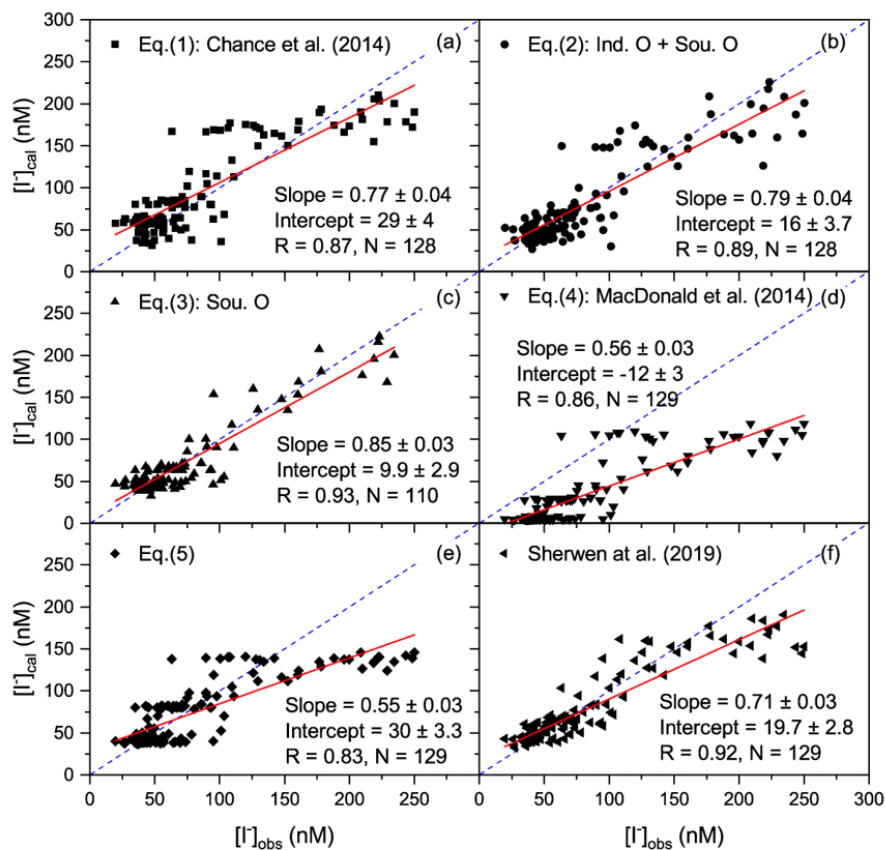
1074



1075

1076 **Figure 5: Latitudinal plot of hourly-averaged field measurements of wind speed, ozone**  
1077 **mixing ratios, SST and salinity<sup>†</sup> from ISOE-8, IIOE-2, and ISOE-9 campaigns. Data**  
1078 **markers in red belong to the IIOE-2 campaign; those in blue belong to the ISOE-8 and**  
1079 **markers in black are from ISOE-9 for all the panels. Observational plots for ISOE-8 and**  
1080 **IIOE-2 were adapted from Mahajan et al. 2019 a & b.**

<sup>†</sup> Salinity data for IIOE-2 are monthly climatological means from World Ocean Atlas as described in the supplementary text.

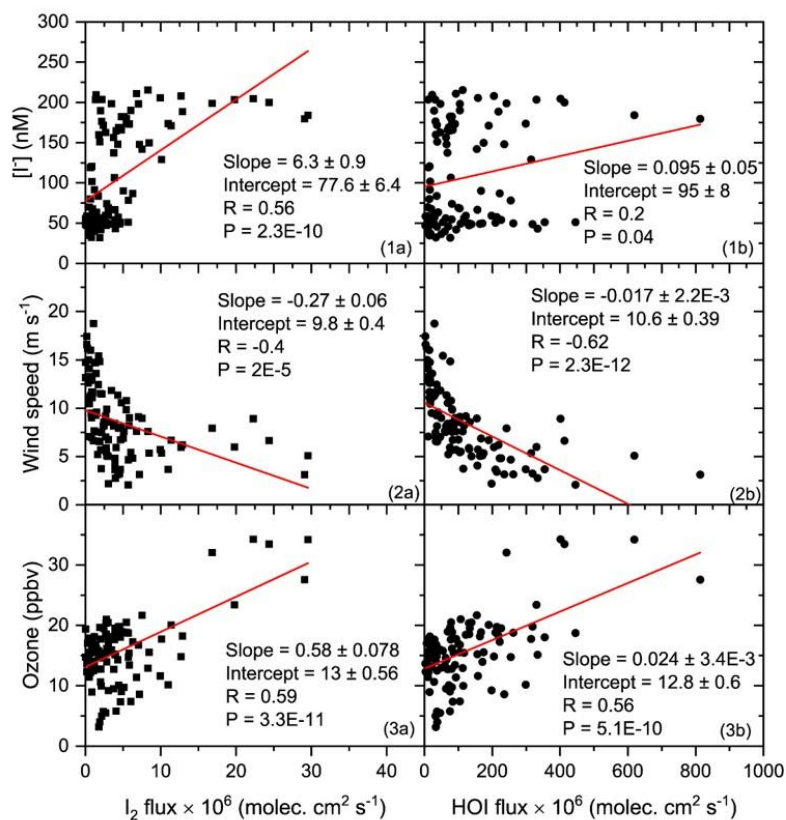


1081

1082 **Figure 6: Linear fit analysis of estimated sea surface iodide (SSI) concentrations (y axis)**  
1083 **from parameterisation methods in Eq. (1) to (5) and model prediction (Sherwen et al.,**  
1084 **2019) against measured SSI concentration (x axis) from ISOE-9, SK-333 and BoBBLE.**  
1085 **In panel (c) SSI are compared only with ISOE-9 observations for Southern Ocean specific**  
1086 **parameterisation. R represents Pearson's correlation coefficient and N is the size of the**  
1087 **dataset. Dashed blue line represents identity (1:1) line.**

1088

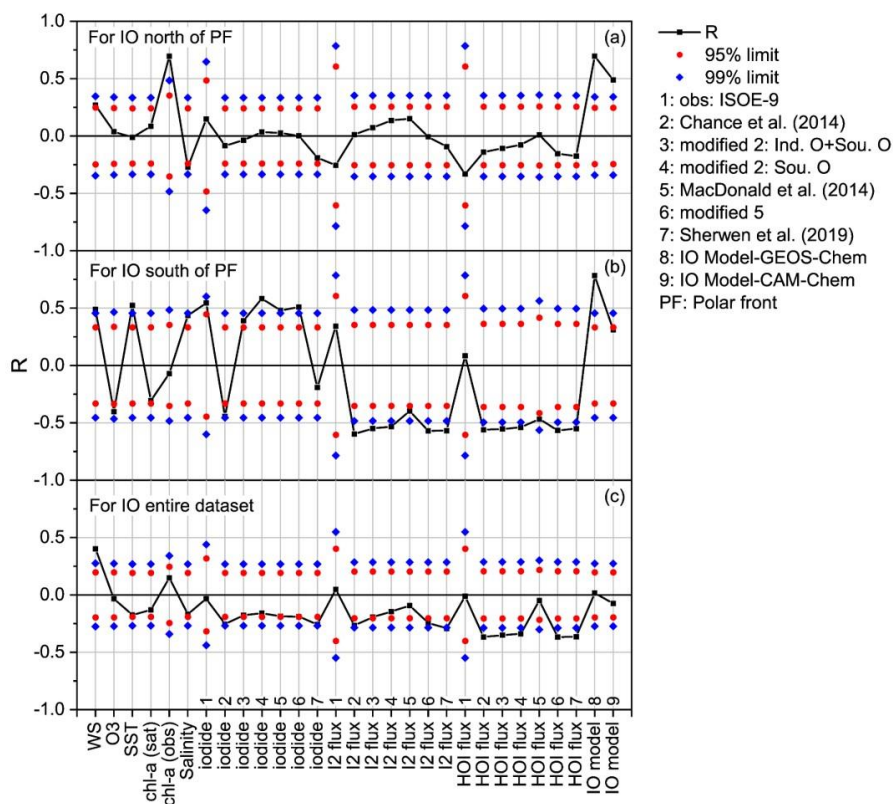
1089



1090

1091 **Figure 7: Linear fit of daily average sea surface iodide (SSI) concentration, wind speed**  
1092 **and ozone mixing ratio (y axis) against calculated I<sub>2</sub> and HOI flux (x axis) against for all**  
1093 **the campaign. HOI and I<sub>2</sub> are calculated using SSI estimated using the modified Chance**  
1094 **parameterisation for Indian Ocean and Southern Ocean in Eq. (2).**

1095



1096

1097 **Figure 8: Pearson's correlation coefficient of observed iodine monoxide (IO) with oceanic**

1098 **and atmospheric parameters combined for ISOE-8, IOE-2, and ISOE-9 campaigns.**

1099 **Correlations are performed for daily averages of IO and corresponding parameters listed**

1100 **on the X axis. The black squares represent Pearson's correlation coefficients (R), the**

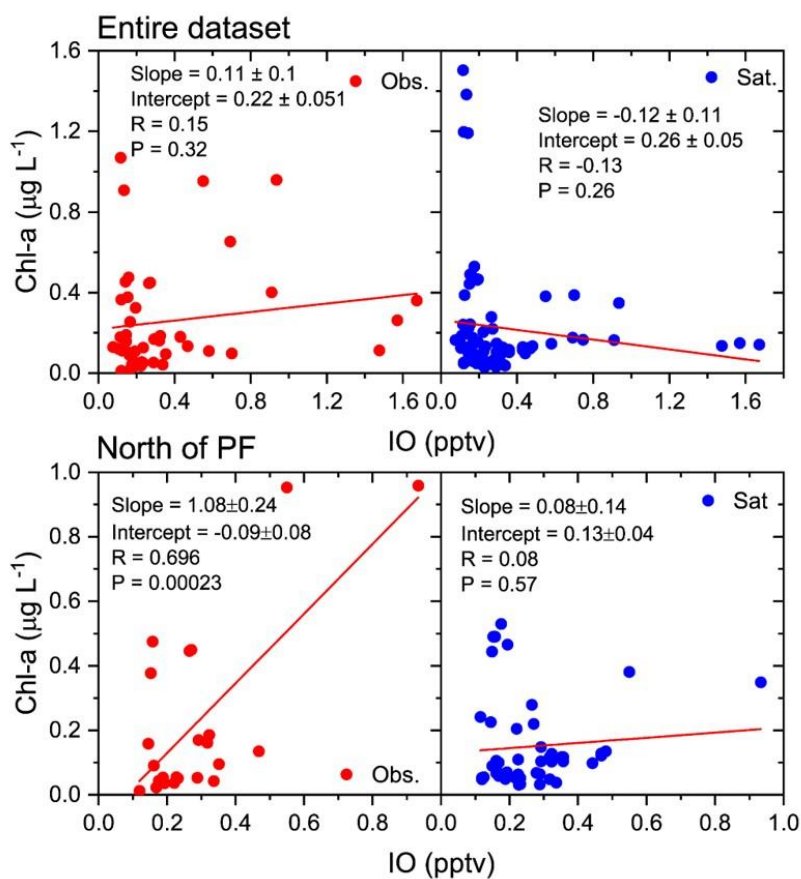
1101 **diamonds (blue) mark the 99% confidence limit, and the circles (red) correspond to the**

1102 **95% confidence limits in all the panels, (a) includes data from all campaigns to the north**

1103 **of the polar front (n = 72), (b) represents combined data for the south of the polar front**

1104 **(n = 48), the last panel (c) includes the entire dataset from three campaigns (n = 120).**

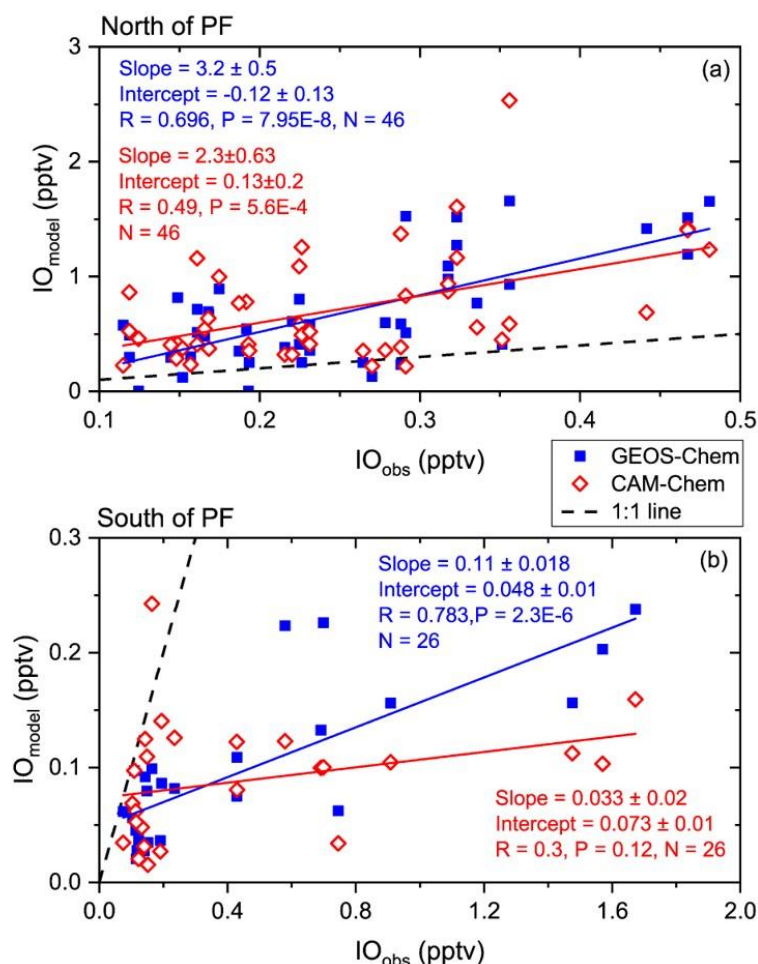
1105



1106

1107 **Figure 9: Linear fit of daily averaged field observations of chlorophyll-*a* (red circles) and**  
1108 **chlorophyll-*a* satellite data (blue circles) (y axis) against observed iodine monoxide (IO)**  
1109 **(x axis) from ISOE-8, HIOE-2, and ISOE-9 campaigns. The top panel includes**  
1110 **chlorophyll-*a* for the entire dataset; the bottom panel includes data to the north of the**  
1111 **polar front.**

1112



1113

1114 **Figure 10: Linear fit of daily averages of modelled surface iodine monoxide (IO) output**  
1115 **(y axis) from GEOS-Chem (filled blue squares) and CAM-Chem (unfilled red diamonds)**  
1116 **against observed IO (x axis) for ISOE-8, IOE-2 and ISOE-9 campaigns. (a) includes**  
1117 **linear fits of both GEOS-Chem and CAM-Chem for IO detected to the north of the polar**  
1118 **front, (b) shows the same for the region south of the polar front. Two data points in panel**  
1119 **(a) at 41° S and 43° S are removed due to large differences between observation and**  
1120 **modelled values.**

1121

1122

1123



1124

1125 **10. Tables**

Expedition	Research Vessel	Duration	Location	Meridional Transect	Observations
8 <sup>th</sup> Indian Southern Ocean Expedition (ISOE-8)	Sagar Nidhi, India	7 Jan 2015 to 22 Feb 2015	Indian Ocean from Chennai, India to Port Louis, Mauritius	13° N to 56° S	IO, O <sub>3</sub>
2 <sup>nd</sup> International Indian Ocean Expedition (IIOE-2)	Sagar Nidhi, India	4 to 22 Dec 2015	Indian Ocean from Goa, India to Port Louis, Mauritius	15° N to 20° S	IO, O <sub>3</sub>
Bay of Bengal Boundary Layer Experiment (BoBBLE)	R.V. Sindhu Sadhana	23 June 2016 to 24 July 2016	Southern Bay of Bengal	8° N to 10° N	Seawater samples for I <sup>-</sup>
Sagar Kanya-333 (SK-333)	Sagar Kanya, India	5 Sept 2016 to 20 Sept 2016	Southern Arabian Sea and Southern Bay of Bengal	1.6° N to 4° S	Seawater samples for I <sup>-</sup>
9 <sup>th</sup> Indian Southern Ocean Expedition (ISOE-9)	S A Agulhas, South Africa	6 Jan 2017 to 26 Feb 2017	Indian and Southern Ocean from Port Louis, Mauritius to Antarctica	20° S to 70° S	IO, O <sub>3</sub> , I <sup>-</sup>

1126

1127 **Table 1: Details of the three expeditions contributing to the IO and seawater iodide**  
 1128 **dataset in this study. Expeditions are listed in chronological order from 2014 to 2016.**

1129

1130



1131

1132

Eq. No	Reference	Parametric equation ([iodide] in nM)	Database location	Data points	R <sup>2*</sup>	R <sup>2</sup>
Eq. 1	<i>Chance et al. (2014)</i>	$[iodide] = 0.28(\pm 0.002) \times sst^2 + 1.7(\pm 0.2) \times  latitude  + 0.9(\pm 0.4) \times [NO_3^-] - 0.02(\pm 0.002) \times MLD_{pt} + 7(\pm 2) \times salinity - 309(\pm 75)$	<i>Majorly Atlantic and Pacific Ocean</i>	<i>n = 673</i>	<i>0.676</i>	<i>0.758</i>
Eq. 2	This study	$[iodide] = 0.36(\pm 0.04) \times sst^2 - 2.7(\pm 0.5) \times  latitude  + 0.28(\pm 0.57) \times [NO_3^-] + 0.64(\pm 0.17) \times MLD_{pt} - 5.4(\pm 3.82) \times salinity + 22(\pm 137)$	Indian and Southern Ocean	n = 128	0.794	0.794 <sup>^</sup>
Eq. 3	This study	$[iodide] = 0.25(\pm 0.017) \times sst^2 - 0.6(\pm 0.4) \times  latitude  + 2.2(\pm 0.4) \times [NO_3^-] - 5.5(\pm 3.3) \times salinity + 212(\pm 123)$	Southern Ocean	n = 110	0.859	0.859 <sup>^</sup>
Eq. 4	<i>MacDonald et al. (2014)</i>	$[iodide] = 1.46 \times 10^{15} \times \exp\left(\frac{-9134}{SST}\right)$	<i>Atlantic, Central and West Pacific Ocean</i>	<i>n = ~88</i>	<i>0.71</i>	<i>0.739</i>
Eq. 5	This study	$[iodide] = 3.6 \times 10^7 \times \exp\left(\frac{-3763}{SST}\right)$	Indian and Southern Ocean	n = 129	0.702	0.697 <sup>^</sup>
Eq. 6	<i>Sherwen et al. (2019)</i>	<i>Machine learning based regression approach</i>	<i>Atlantic, Pacific, Indian and Southern Oceans</i>	<i>n = 1293</i>	-	<i>0.842</i>

1133

1134 **Table 2: List of existing global (italics) and new region-specific (regular)**  
 1135 **parameterisations for sea surface iodide concentration indicating data location and**  
 1136 **number of data points used to formulate each equation. Here [iodide] represents sea**  
 1137 **surface iodide concentration in nM, sea surface temperature as ‘sst’ in °C, and SST in K.**  
 1138 **Nitrate concentration ([NO<sub>3</sub><sup>-</sup>]) is given in μmol L<sup>-1</sup>, mixed layer depth as MLD<sub>pt</sub> in m,**  
 1139 **subscript ‘pt’ indicates potential temperature implying a temperature change of 0.5 °C**  
 1140 **from the ocean surface (Monterey and Levitus, 1997), and salinity in PSU. Further details**  
 1141 **on individual parameters and the choice of Eq. (1) over others proposed in Chance et al.**  
 1142 **(2014) are discussed further in the supplementary text. R<sup>2\*</sup> represents the initial**  
 1143 **coefficient of determination (COD) while deriving each parameterisation, and R<sup>2</sup>**  
 1144 **represents COD from correlation analysis of the calculated iodide with observations in**  
 1145 **this study (ISOE-9, SK-333, BoBBLE).**





1146 **^Higher  $R^2$  values for the modified parameterisations reflect the fact that they have been**  
1147 **derived using the same observational data as they are tested on.**